2013

# Feasibility Study of In-situ Characterization of Size Distribution of Air Voids in Concrete Pavements

Kai Ming Li
*Ray W. Herrick Laboratories, Purdue University*, mmkmli@purdue.edu

Bao N. Tong
*Purdue University*, bntong@purdue.edu

Sheng Liu
*Purdue University*, liu178@purdue.edu

Recommended Citation
Li, K., B. N. Tong, and S. Liu. *Feasibility Study of In-situ Characterization of Size Distribution of Air Voids in Concrete Pavements*. Publication FHWA/IN/JTRP-2013/10. Joint Transportation Research Program, Indiana Department of Transportation and Purdue University, West Lafayette, Indiana, 2013. doi: 10.5703/1288284315212.

JOINT TRANSPORTATION
RESEARCH PROGRAM
INDIANA DEPARTMENT OF TRANSPORTATION
AND PURDUE UNIVERSITY

# Feasibility Study of In-situ Characterization of Size Distribution of Air Voids in Concrete Pavements

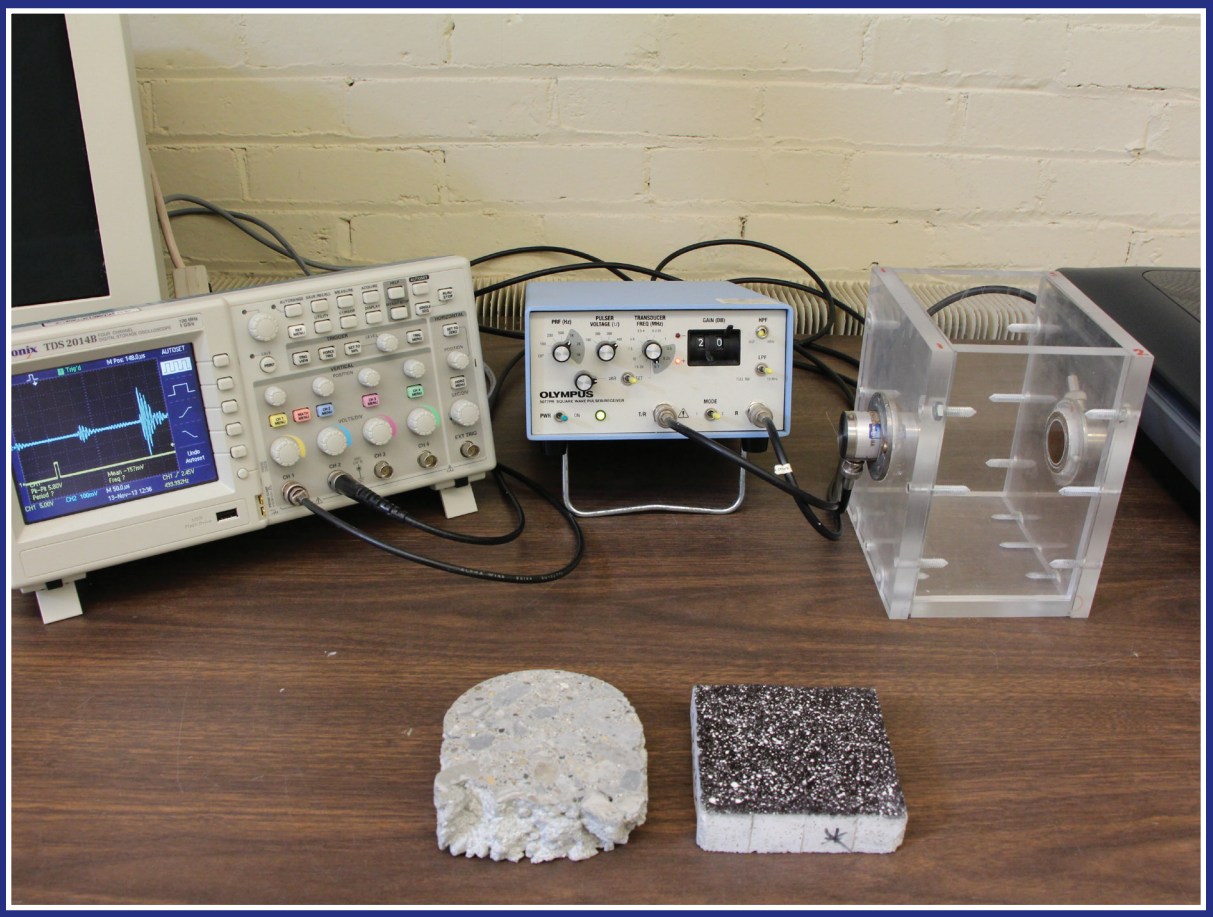


Kai Ming Li

Bao N. Tong

Sheng Liu

SPR-3473 • Report Number: FHWA/IN/JTRP-2013/10 • DOI: 10.5703/1288284315212

## RECOMMENDED CITATION

Li, K. M., B. N. Tong, and S. Liu. *Feasibility Study of In-situ Characterization of Size Distribution of Air Voids in Concrete Pavements*. Publication FHWA/IN/JTRP-2013/10. Joint Transportation Research Program, Indiana Department of Transportation and Purdue University, West Lafayette, Indiana, 2013. doi: 10.5703/1288284315212.

## AUTHORS

**Kai Ming Li, PhD**
Professor of Mechanical Engineering
Ray W. Herrick Laboratories
School of Mechanical Engineering
Purdue University
(765) 494-1099
mmkmli@purdue.edu
*Corresponding Author*

**Bao N. Tong**
Graduate Research Assistant
Ray W. Herrick Laboratories
School of Mechanical Engineering
Purdue University

**Sheng Liu**
Graduate Research Assistant
Ray W. Herrick Laboratories
School of Mechanical Engineering
Purdue University

## ACKNOWLEDGMENTS

This work was funded by Joint Transportation Research Porgram under the Grant No. SPR-3473. The authors gratefully acknowledge Dr. Tommy Nantung, the research manager of INDOT, for his encouragement in the past years. We would like to thank Hsu Chew Lee, Hongdan Tao, Matt Blevins, and Trevor Brown for their help in conducting the experiments. We would also thank Steve Dick of INDOT for providing technical support.

## JOINT TRANSPORTATION RESEARCH PROGRAM

The Joint Transportation Research Program serves as a vehicle for INDOT collaboration with higher education institutions and industry in Indiana to facilitate innovation that results in continuous improvement in the planning, design, construction, operation, management and economic efficiency of the Indiana transportation infrastructure. https://engineering.purdue.edu/JTRP/index_html

Published reports of the Joint Transportation Research Program are available at: http://docs.lib.purdue.edu/jtrp/

## NOTICE

**TECHNICAL REPORT STANDARD TITLE PAGE**

| 1. Report No. | 2. Government Accession No. | 3. Recipient's Catalog No. |
|---|---|---|
| FHWA/IN/JTRP-2013/10 | | |

| 4. Title and Subtitle | 5. Report Date |
|---|---|
| Feasibility Study of In-situ Characterization of Size Distribution of Air-voids in Concrete Pavements | June 2013 |
| | 6. Performing Organization Code |
| 7. Author(s) | 8. Performing Organization Report No. |
| Kai Ming Li , Bao N. Tong , Sheng Liu | FHWA/IN/JTRP-2013/10 |
| 9. Performing Organization Name and Address | 10. Work Unit No. |
| Joint Transportation Research Program<br>Purdue University<br>550 Stadium Mall Drive<br>West Lafayette, IN 47907-2051 | |
| | 11. Contract or Grant No. |
| | SPR-3473 |
| 12. Sponsoring Agency Name and Address | 13. Type of Report and Period Covered |
| Indiana Department of Transportation<br>State Office Building<br>100 North Senate Avenue<br>Indianapolis, IN 46204 | Final Report |
| | 14. Sponsoring Agency Code |

**15. Supplementary Notes**

Prepared in cooperation with the Indiana Department of Transportation and Federal Highway Administration.

**16. Abstract**

This report concerns a feasibility study on the use of a non-destructive and non-invasive method to determine the size distribution of air voids in fresh concrete, which will be used for laying concrete pavement. A preliminary review of different techniques suggested that the measurement of the p-wave velocity of ultrasound pulses transmitted through a fresh concrete specimen offers the most straightforward approach. This report describes an experimental study to address the design of an experimental test rig, the selection of appropriate equipment, and the determination of the p-wave velocity in fresh cementitious materials. The paper starts with the ultrasound characterization of fresh cement and mortars. Then, the feasibility of using the ultrasound method to determine the air-void content in a fresh concrete specimen with a minimum thickness of 4" is examined. In addition to the discussions of the ultrasound characterization of fresh cementitious materials, this paper also reports on the development of a suite of MATLAB programs to characterize the air-void systems of hardened cementitious materials. The approach is based on image processing techniques used to analyze digital images of polished specimens collected with a flatbed scanner. The results will provide pertinent information on the air-void systems in hardened cementititous materials.

| 17. Key Words | 18. Distribution Statement |
|---|---|
| fresh mortar, fresh concrete, ultrasonic, monitoring, air-voids | No restrictions. This document is available to the public through the National Technical Information Service, Springfield, VA 22161. |

| 19. Security Classif. (of this report) | 20. Security Classif. (of this page) | 21. No. of Pages | 22. Price |
|---|---|---|---|
| Unclassified | Unclassified | 35 | |

**Form DOT F 1700.7 (8-69)**

## EXECUTIVE SUMMARY

# FEASIBILITY STUDY OF IN-SITU CHARACTERIZATION OF SIZE DISTRIBUTION OF AIR VOIDS IN CONCRETE PAVEMENTS

## Introduction

The air-void system is known to improve the frost resistance of hardened concrete in a region with a cold climate. Extensive laboratory experiments and long-term field trials have confirmed that concrete containing properly entrained air has a better resistance to damage arising from freezing and thawing due to internal distress and salt scaling. To achieve the targeted result, a large number of smaller size bubbles are needed in these air-void systems. It is, therefore, important to control the geometrical characteristics of the bubbles and, in particular, the bubble size distribution. Although the air entrainment mechanism is well known and the procedures for introducing air-entraining admixtures in highway concrete are well established, developing consistent air-void systems in concrete is still a challenging task.

The current measurement technique does not provide timely results that can be used for preventing marginal air-void systems in concrete materials from being placed in the field. In many cases, by the time the air-void system results were known, it was too late to take remedial actions such as the remove-and-replace option, which have presented disadvantages to INDOT and its contractors in terms of both time and money. A feasibility study was proposed to investigate the use of a non-invasive method to accurately determine the spacing factor, distribution of air voids, and how the air-void system of fresh concrete changes over time. In particular, a possible use of ultrasound as a non-invasive means was used to tackle this major challenge in the concrete industry.

## Findings

- The ultimate goal of this feasibility study was to identify whether fresh concrete specimens can be characterized within the first hour after the concrete is mixed. Based on the results obtained from the available instrumentation, the largest sample thickness for signal transmission is of the order of 0.6". For fresh mortar specimens, this sample thickness may be acceptable. However, this thickness is not acceptable for a fresh concrete specimen. This is because the minimum sample thickness needs to be several times larger than the characteristic length scale of the aggregate to obtain a representative sampling.
- The latest experimental setup demonstrated the feasibility of using a step-up transformer and a set of tuned transducers to significantly increase the time-domain signal amplitude at minimal additional costs. To overcome the signal quality issues encountered, larger active area transducers with higher amplitude outputs might be sourced. Although the desired sample thickness of 4" was not achieved during the first two hours of hydration, this sample thickness constraint may be relaxed by switching to a larger active area transducer. The effective result would be sampling a comparable volume of the test specimen, but at a lower sample thickness.
- Another goal of the project was the development of image processing techniques for air-void systems in hardened concrete during the refinement process in the design of the experimental test fixture. No conclusive time-domain results were obtained within the first few hours of cement hydration. On the other hand, more reliable data were recorded beyond this time window.
- Based on the numerical results obtained from the developed computer program, expanded capabilities can be addressed by processing the entire high-resolution image. These capabilities may reduce the time and effort needed to prepare each specimen for air-void analysis. In turn, more specimens can be analyzed to generate statistically representative predictions. Preliminary results show promise that a coarse aggregate in hardened concrete identification filter based on high sensitivity edge detection combined with color image enhancement techniques would yield a semi-automatic classification system. The image processing algorithms can also be applied to other optical characterization projects for the estimation of other pertinent parameters of cementitious materials.

## Implementation

This report concerns a feasibility study on the use of a non-destructive and non-invasive method to determine the size distribution of air voids in fresh concrete, which will be used for placing and acceptance of concrete pavement. A preliminary review of different techniques suggested that the measurement of the p-wave velocity of ultrasound pulses transmitted through a fresh concrete specimen offers the most straightforward approach. This report describes an experimental study to address the design of an experimental test rig, the selection of appropriate equipment, and the determination of the p-wave velocity in fresh cementitious materials. The ultrasound characterization of fresh cement and mortars are discussed. Then, the feasibility of using the ultrasound method to determine the air-void content in a fresh concrete specimen with a minimum thickness of 4" is examined. In addition to the discussions of the ultrasound characterization of fresh cementitious materials, this study also explores the development of a suite of computer programs to characterize the air-void systems of hardened cementitious materials. The approach is based on image processing techniques used to analyze digital images of polished specimens collected with a flatbed scanner. The results will provide pertinent information on the air-void systems in hardened cementitious materials. The state-of-the-art image processing technique has been applied to examine digital images of polished specimens collected with a flatbed scanner. Implementation of the software program and the coloring technique in the hardened concrete is very suitable for fast air-void system investigation of hardened concrete.

CONTENTS

# LIST OF TABLES

# LIST OF FIGURES

# 1. INTRODUCTION

## 1.1 Motivation of the Current Study

The Indiana Department of Transport (INDOT) encountered an issue with pavement durability in the northern part of Indiana. Both asphalt and concrete pavements exhibited these durability issues. A section (located north of South Bend in Roseland) of Indiana State Road SR-933 was found to suffer from serious deterioration at the concrete pavement joints. This deterioration was so deleterious that the safety of the traveling public was compromised (see Figure 1.1). The cost of rehabilitating this section of SR-933 was $3.37 million in 2008. A preliminary investigation conducted by INDOT confirmed that the premature failure of the joints was largely due to the repeated freezing and thawing cycles during the winter months.

This premature failure of the pavement's joints also attracted the attention of the Federal Highway Administration (FHWA). They initiated an independent investigation aiming to determine the main causes of this type of deterioration. The FHWA and INDOT studies related to the road section of SR-933 both concluded that the main cause of the deterioration was the filling of the air voids with a secondary cement hydration product. In many cases, the air-void system was compromised because of a lack of smaller air bubbles in the concrete pavements. More specifically, exposure to freezing wintry conditions and a lack of small air voids made the concrete pavements more susceptible to damage caused by the repeated freezing of water. In the past, road sections in other states (mainly Kansas and Iowa) have exhibited a similar problem as isolated events on a smaller scale. The problem of premature failure at road sections prompted a change in the specification of the air-void systems for the fresh concrete used in these two states which is the main motivation of the current study.

**Figure 1.1** Joint deteriorations at section of Indiana State Road SR-933.

## 1.2 Background

For many decades, the entrainment of air voids was known to improve the frost resistance of hardened concrete in a region with cold climate (*1*). Extensive laboratory experiments and long-term field trials have confirmed that concrete containing properly entrained air has better resistance to damage arising from freezing and thawing due to internal distress and salt scaling. To achieve the targeted result, a large number of smaller size bubbles are needed in these air-void systems (i.e., it is important to control the geometrical characteristics of the bubbles and, in particular, the bubble size distribution) (*2*). Although the air entrainment mechanism is well known (*3*) and the procedures for introducing air-entraining admixtures in highway concrete are well established, developing consistent air-void systems in concrete is still a challenging task.

Powers (*2,4*) characterized the air voids using a spacing factor, which forms the basis for predicting the freeze-thaw performance of concrete. This spacing factor is defined as the maximum distance from any point in the cement paste to an air-void boundary. Published experimental data validate the use of this spacing factor for predicting the frost resistance of concrete. In addition, Snyder (*5*) conducted numerical experiments comparing various models (*6–8*) for predicting the spacing factor and, consequently, the freeze-thaw performance. Many of these numerical models can be validated by comparing the air-void parameters with detailed experimental measurements (*9,10*) of the spacing factor and size distribution of the air voids.

In general, specifying the use of air-entrained concrete for its resistance to freezing and thawing has been common practice (*11*). However, the premature failure of hardened concrete is still a recurring problem because of inadequate air entrainment (*12*). The current practice for delivering concrete to a job site normally specifies the total air content for entrainment. This is because, according to the ASTM C 457 Standard Test Method (*13*), the determination of the air-void spacing factor is conducted in hardened concrete by the linear traverse method using a microscope. This method requires a sample of concrete cored on-site. The concrete is then sliced, ground, and lapped in the laboratory to determine the spacing factor, total air content, and specific surface (the ratio of the surface area of the air voids to their volume). These measurement procedures are usually conducted manually, although other automated image analysis systems are now available (*14,15*). The microscopic determination of the air-void spacing factor is a tedious task. Preferably, the air-void distribution in fresh concrete should be determined during the pouring of the concrete to prevent contractors from pouring concrete with an inadequate air-void system.

The setting process for concrete is noteworthy and can be summarized briefly as follows. A chemical reaction starts when the cement is mixed with water to form mortar. This mortar, which may be modeled as a

thixotropic fluid, changes slowly and bonds aggregate particles together to form hardened concrete over a period of time. Fresh concrete will begin the initial setting process within the first 30 min. Therefore, there is a small window of opportunity to accurately measure the small void properties to ensure that a QC/QA concrete will have the bubble spacing required to protect the concrete in service. This is also of interest to INDOT and its contractors, to ensure that quality concrete is placed in the field to avoid penalties and concrete replacement, which will delay a project and increase its cost. However, it is extremely difficult to measure the size distribution of air voids in fresh concrete on-site. On the other hand, the total air content of fresh concrete can be easily and quickly measured directly using a pressure meter. As a result, most standards for practical quality control often rely on the use of the total air content in fresh concrete without a detailed specification of the size distribution of the air voids.

There is a disadvantage in specifying the total air content in fresh concrete. Recent studies have indicated that an acceptable air content limit does not necessarily lead to an adequate spacing factor in fresh concrete (*16*). This is because larger air voids (which are more compressible) tend to exhibit larger adverse effects on the freeze/thaw resistance than smaller voids. Consequently, low air content, as measured by a pressure meter, may mean that most of the air voids are small and the frost protection is sufficient. Conversely, a compliant air content measurement for fresh concrete may indicate a small number of large voids, which do not provide effective protection against frost. Indeed, measurement results have suggested that all the field concrete samples that show poor frost resistances have unsatisfactory spacing factors, even though their air content is within the recommended limits.

To overcome these problems regarding air-void systems in fresh concrete, an apparatus known as the air void analyzer (AVA) was developed in the 1990s to measure the air-void parameters of fresh concrete containing entrained air (*17*). The working principle of this device is as follows. Using a specially designed tool, a sample of paste is taken from the fresh concrete. The sample is then injected into a layer of viscous liquid, which helps prevent the collapse or coalescence of air bubbles during mixing. Air voids of different sizes will rise through a column of water at different rates: larger bubbles will rise faster and smaller bubbles will rise slower. The rising air bubbles strike a buoyancy plate, at which point the size distribution of the air voids can be determined by analyzing the change in the buoyancy of the plate over time. With the AVA, fresh concrete can be analyzed in about 20 min, yielding both the spacing factor and specific surface area. However, this method and other proposed methods are invasive in nature; drawing a sample from the fresh concrete will inevitably affect the composition of the original paste. As a result, there is currently no reliable method for producing repeatable and reproducible results to quantify the size and distribution of the air voids in fresh concrete.

The current measurement technique does not provide timely results that can be used for preventing low-quality concrete materials from being placed in the field. In many cases, by the time the air-void system results were known, it was too late to take remedial actions such as the remove-and-replace option, which have presented disadvantages to INDOT and its contractors in terms of both time and money. We therefore propose a feasibility study to investigate the use of a non-invasive method to accurately determine the spacing factor, distribution of air voids, and how the air-void system of fresh concrete changes over time. In particular, we wish to examine the use of ultrasound as a non-invasive means to tackle this major challenge in the concrete industry. The proposed project will examine the feasibility of using ultrasonic characterization methods for fresh concrete to estimate the size distribution of air voids and determine the spacing factor. In particular, the p-wave velocity for the ultrasound transmitted through a specimen will be measured at different time intervals during the hydrating period, which can be used to monitor the change in the air-void system of fresh concrete. This information will form the basis for calculating the spacing factor and specific surface of the air voids in the hardened concrete.

### 1.3 Ultrasonic Characterization Techniques

Generally speaking, ultrasonic characterization techniques have traditionally been used for directly measuring mechanical properties and assessing member thickness, stiffness, crackling, and delamination in hardened concrete applications (*18,19*). More recent studies have used ultrasound techniques to quantify the amount of air voids in both hardened concrete (*20–22*) and fresh cement pastes (*23,24*). The ultrasonic techniques have also been used for the prognostic and diagnostic monitoring of near surface concrete (*25*).

Concrete is composed of a mixture of cement, sand, water, and coarse aggregate. The particle size distributions in the mixture can vary by several orders of magnitude depending on the composition of the aggregate materials. Typical ultrasonic studies on fresh concrete specimens are usually performed on the cement paste or mortar mix (sand, cement, and water) because of the high attenuation of the ultrasonic waves transmitted through specimens during the first few hours of the setting process. The attenuation and dispersion of ultrasound waves are even higher in concrete specimens because of the presence of aggregates. Mortar and concrete also contain pores and/or capillaries, which range in size from about a nanometer to a few millimeters. The physical properties of the mixed phases (solid, liquid, and gas) found in fresh concrete make its ultrasonic characterization a challenging task. Furthermore, the sizes and scales of various features of the fresh concrete are strongly affected by

the frequencies used in the study of the ultrasound waves transmitted through the specimens.

In a recent study (*26*), pulse-burst ultrasound signals with a frequency range between 500 kHz and 5 MHZ were used to characterize the entrained air voids in hardened cement paste. For a cement matrix with no embedded air voids, weak dispersions of longitudinal (p-wave) and transverse waves were observed experimentally in the frequency range of interest (500 kHz to 5 MHz), i.e., the measured phase velocities were constant. However, the corresponding attenuation coefficients were shown to increase linearly with an increase in frequency. Using tone-burst signals with central frequencies varying from 20 kHz to 1 MHz, Aggelis et al. (*27*) measured the dispersive and attenuative characteristics of fresh mortar with various sand contents by volume and different water to cement (*w*/*c*) ratios. The attenuation coefficients at various center frequencies were measured at different sand contents. Experimental data indicated that the attenuation increased linearly with an increase in the sand content. On the other hand, the measured phase velocity of the p-wave was relatively independent of the sand content. Aggelis et al. (*27*) further concluded that the size of the sand in the mortar and the sand content dominated the attenuation coefficient of the transmitted p-wave. The effect of the entrapped air bubbles, which increased the phase velocity of the p-wave, was more noticeable at lower frequencies. Larger air voids of the order of 2.8 mm can be achieved by adding expanded polystyrene spheres to the cement-paste matrix (*28*). The effects of air voids and small sand particles on the p-wave velocity and/or attenuation factor of the hardened concrete have been shown to be small (both experimentally and theoretically) at ultrasound frequencies below 500 kHz.

In an experimental study, Philippidis and Aggelis (*19*) used narrowband ultrasound pulses with different frequencies from 15 kHz to 1 MHz to study the acoustic characteristics of hardened cementitious materials. In particular, cement paste, mortar, and concrete specimens were used for these experiments. It was concluded that the effect of the *w*/*c* ratio on the propagation behavior was the most prominent for cement paste and mortar. The effect of the aggregate size, on the other hand, was the most important for the propagation of ultrasound through mortar and concrete. The effect on the attenuation coefficient was more significant than that on the pulse velocity. They further suggested that a source frequency of 100 KHz or above should be used when ultrasonic techniques are used to examine the effect of the *w*/c ratio, aggregate-to-cement ratio, and aggregate fineness.

The basic configuration for a test rig, which was initially proposed by Reinhardt et al. (*29,30*), involves a through-transmission setup for the ultrasonic monitoring of fresh cement paste. A cementitious specimen is placed between a pair of acrylic plates separated by an elastomeric spacer. An ultrasound transducer is attached to each of the two parallel plates. The first transducer serves as a sound source emitting ultrasound waves, whereas the second transducer is a receiver that collects the signals transmitted through the specimen cast in the test rig. Another test configuration is a pulse-echo system (*31*) that uses a single transducer that serves as both the source and receiver. The arrival time of the echo signal is measured, and the depth of the reflecting interface is determined using the known wave velocities in the propagation medium. A similar approach is known as the ultrasonic wave reflection (UWR) method, which calculates the amplitudes of the echo signals and determines the reflection coefficient with respect to a buffer material (whose properties are known) (*21,31*). The reflection occurs at the interface of the buffer material (e.g., a steel plate) and the cement-based specimen.

In its liquid state, the cementitious specimen does not support the propagation of shear waves. Hence, the pulse is reflected almost entirely at the buffer material and cementitious interface. As the cementitious specimen hardens, shear waves are able to propagate through the fresh cement. This leads to a lower reflected signal amplitude from scattering at the interface. Only a fraction of a millimeter of the test specimen thickness is of significance in the determination of the reflection coefficient (*21*). The UWR method was not selected for the feasibility study because air voids deeper than the first few millimeters are of interest.

To monitor more of the test specimen, Kim et al. (*21*) applied the vibrational resonant frequencies method, based on Kolluru et al. (*32*). This method relies on the measurement of the first two resonant frequencies using an impact-induced vibration source. The elastic modulus and Poisson's ratio are determined via a Rayleigh-Ritz analysis. These parameters can be related to the air content in the test specimen. Kim et al.'s (*21*) results indicate that the UWR and vibrational resonance frequency monitoring methods generate similar predictions after the first 6 h (when the resonance data was acquired). It is important to note that the UWR method tends to only measure the effects of mortar within the first fraction of a millimeter in fresh concrete. The vibrational resonance frequency method measured the average properties of a 6"-thick test specimen that contained aggregate material (i.e., mixed phases). However, the vibrational resonance frequency method was not selected for two reasons. First, this method requires a *w*/*c* ratio of at least 0.5 to achieve a good signal. Second, early detection times (within the first 30 min of mixing) are desired, where the cementitious specimens are still in the liquid phase with a high damping factor. Interestingly, Kim et al.'s results indicate that mortar specimens appear to be homogeneous, even in the submillimeter scale.

Sayers and Grenfell (*33*) used the ultrasonic transmission of compressional and shear waves to monitor the change in the mechanical properties of hydrating cement. Their tests demonstrated that the critical development of the mechanical properties in cement occurred within the first few hours of curing. It was

shown that the waveforms of the ultrasonic pulses changed with time as the specimen cured. Experimental tests conducted by Sayers and Dahlin (*34*) determined that ultrasonic wave propagation during the first few hours of hydration was sensitive to air inclusions in the cement paste. Air was added to the specimens via the addition of an air entrainment agent (AEA) such as calcium chloride. In Sayers and Dahlin's studies, specimens with higher air concentrations tended to transmit higher frequency components during the early hours of hydration compared to specimens prepared with no added AEA. In other words, the cements pastes with higher air contents were found to act as high-pass filters over the frequency range of interest.

Aggelis et al. (*27,35*) investigated the effects of the *w*/*c* ratios in cement and mortar mixtures throughout the hydration process. Different signal transmission characteristics were identified in a comparison between wave propagation through a solid medium (in hardened concrete) and that through a fluid paste (in the plastic phase). Several different excitation methods such as tone bursts and sinusoidal frequency sweeps were employed. The tone bursts highlighted the strong dispersion behavior of fresh mortar. The sine sweep was used to study the attenuation rate of the test specimen at various excitation frequencies. The results showed that the sand content and grain size had a large influence on the wave parameters during the early stages of hydration. Air voids tended to dominate the attenuation rate at low frequencies because strong attenuation rates were experienced in the cement paste even in the absence of sand.

Kmack et al. (*23*) provided a more recent example of the ultrasonic characterization of fresh concrete specimens. In their study, various amounts of AEA (0.0% up to 0.6% by weight of cement) were tested using the through-transmission test configuration on a thin specimen of mortar. The samples were monitored and waveforms were recorded at 5-min increments during the first 6 h. Monitoring continued beyond 12 h of setting. The sample thickness for most of the experiments was around 1.20 cm to ensure the transmission of an observable signal during the first 20 min.

An experimental study conducted by Kmack et al. (*23*) provided the most relevant reference for the present study. In their experiments, Kmack et al. used a matching pair of transducers (1 MHz nominal center frequency) to conduct the through-transmission experiments on hydrating cements with and without AEA during the first 12 h after mixing the cement with water. Up to 0.6% (by cement mass) of AEA was added to the cement paste (a thickness of 12 mm) with different *w*/*c* ratios. The experimental results showed that the differences between a specimen containing AEA and one with no additive were clearly distinguishable based on the amplitude differences in the p-wave velocity and the peak-to-peak signal amplitudes. The addition of AEA apparently suppressed the peak-to-peak signal strength, pulse velocity, and peak frequency in the fresh cement paste (*23*).

An alternative approach for ultrasonic characterization employs surface acoustic wave measurements (*25,26,37*). These waves can be used to characterize the first few centimeters of a test specimen using a sensor positioned on the free surface. This is especially convenient for on-site applications where access to through-transmission measurement is unlikely. Parameters such as Young's modulus and Poisson's ratio have been extracted from low frequency (50 kHz) measurements using standard compression wave transducers for monitoring the Rayleigh waves. Wedge-shaped transducers can be employed for increased performance. Lasers could also be used to generate and detect Rayleigh waves, which would allow non-contact measurements to be performed over a frequency range of 200 kHz to 1 MHz. These non-contact measurements would allow the additional flexibility of monitoring several sampling locations at once. A two-dimensional image of the free surface of a test specimen can be visualized by using a scanning laser vibrometer (*38*). This approach is especially relevant when validating numerical propagation models, and in understanding the phenomena of wave propagation at a smaller scale.

The surface wave measurement techniques were not adopted in the feasibility study because of the advanced signal processing requirements involved in isolating the coherent and incoherent signals for extracting relevant measureable physical parameters. Additionally, the characterization of coarse aggregate specimens may require penetration depths deeper than a few centimeters during the first few hours of setting. Because there are several different sources for the scattering of acoustic energy, the isolation of those caused by porosity or viscoelasticity can be difficult to achieve without a complete theory for the multiple scatterings produced by the heterogeneities present in the test specimen. A numerical model for elastic wave propagation in concrete can be found in Ref. (*39*).

In its plastic phase, a cement mixture is highly attenuative. The typical loss mechanisms for wave propagation are material absorption, scattering, and geometric spreading. Material absorption refers to the energy dissipated as heat when a fluid medium interacts with ultrasound waves. This viscoelastic effect tends to be frequency dependent and scales as the square of the frequency. Scattering occurs at the boundaries between materials with different elastic properties. The differences can be associated with the grain structure, multiple phase interactions, precipitates, crystal defects from dislocations, etc. (*23*). Scattering tends to be effective when the size scale of the wave disturbance is on the same order of magnitude as the object of interest. On the other hand, geometric spreading depends on the wave mode and source geometry, which is independent of frequency. For example, spherical longitudinal waves are attenuated by a factor of $1/r$ because of spherical spreading (where $r$ is the distance between the observer and point source).

The determination of the air content using ultrasonic methods appears to be well established for hardened

concrete and fresh specimens that have been hydrated for more than 6 h. However, it is not yet clear whether the characterization of the air-void size and spacing can be obtained using ultrasonic methods because of the influence of the multiphase, multi-size-scale composition of fresh concrete. The aim of the present feasibility study is to determine the sets of experimental conditions required to perform ultrasonic testing on more realistic test specimens using the through-transmission test configuration, and to correlate the phenomena experienced within the first several hours of hydration to the air-void contents.

### 1.4 Optical Image Processing Techniques

Typically, the air-void content of concrete is measured in the field using the "Pressure Method" described in ASTM C231-04 (*40*) or the "Volumetric Method" outlined in ASTM C173-01 (*41*). The "Gravimetric Method" in ASTM C138-01a (*42*) may also be applied in a laboratory environment. Each of these measurement methods requires a separate test specimen that has been prepared using materials from the same concrete mixture. In the preparation of the concrete specimens used in ultrasound measurements, more processing steps are often involved than when using the three ASTM standards described above. These discrepancies in the techniques for preparing specimens may invalidate the results obtained by the ultrasound methods when they are compared with those of the three ASTM standards. A more precise method is desirable to provide an accurate calibration of the measured air-void systems in concrete specimens, by means of the ultrasound method.

It is well known that ASTM C 457 (*13*) establishes a standard to analyze the air-void system in hardened concrete. With the aid of a stereo-optical microscope and an operator, there are three main types of methods described in the standards, as follows:

(1) linear traverse,
(2) modified point-count, and
(3) image analysis.

The procedures for the non-electronic types of equipment are outlined in ASTM C 457. Nevertheless, Walker et al (*43*) pointed out that none of these methods can provide an accurate error bound for the measurements, and it is not known which method generates the most accurate results. More details of these three main methods can be found in Ref. (*43*). In the first two methods, the analysis invariably relies on the operator's ability to detect the air voids at interval points on a sampling grid. Consequently, the process can be time consuming, and the accuracy of the analysis is subject to the skill of the operator.

In contrast, the image analysis method requires less operator time because a computer is typically used to perform the examination instead of a human operator. ASTM C 457 stipulates that its principles must be adhered to in the operation procedures if automatic devices (e.g., electric or electronic counters, totalizers and calculators, computers) are used. Furthermore, the calculation of the same parameters for an air-void system must be performed using the same set of data.

In recent years, many automated methods have been developed using a flatbed scanner or moving microscope stage to address the inadequate sampling of a specimen surface with good results (*44*). A commercial system known as Rapid Air 457 (*45*) is commonly used in Nordic countries to automate the data acquisition using a moving stage and digital microscope. The concrete specimens are sectioned, ground, polished, and then contrasted with black ink. A white powder and/or paste indicator is compacted into the air voids, and the excess material is removed. Prior to image acquisition, the remaining voids in the aggregate and cracks are blackened again. A microscope equipped with a camera system is used to collect multiple snapshots at various positions on the prepared surface to compose a mosaic representation of the specimen. The content of the paste needs to be assumed or computed based on the composition of the mixture prior to the analysis. The parameters of the air-void system are then computed using image processing software.

High-resolution images can be acquired by using a flatbed scanner. The ASTM C 457 standard suggests that a minimum resolution of 3,175 dpi is required for the scanner to ensure a pixel size of about 8 microns. Higher resolution images allow the detection of microscale air voids. Because this type of image analysis system is more sensitive than the human eye, smaller air voids can be detected more consistently and the spacing factor computed by the automated system tends to be lower than those obtained via the manual approach.

To use grayscale processing techniques, a threshold level must be selected. In an 8-bit grayscale image, there are 255 different gray levels. Black corresponds to a level of 0 and white corresponds to a level of 255. The threshold level establishes a specific gray level as the minimum level for a pixel on the scanned image to be classified as an air void. A calibration strip with a black and white indicator strip is placed next to the specimen prior to scanning. Then, the grayscale image is stretched linearly based on the deepest black and brightest white levels detected. This process compensates for slight level variations between scans. Peterson et al. (*50*) presented a systematic method for selecting the threshold level automatically based on an optimal set of parameters. They also used a watershed filter to separate adjacent air voids. The total air content and void frequency were determined by combining the number of air-void intercepts and the total length of the linear traverse test line.

Optical processing techniques performed on a hardened sample can provide a more consistent method for characterizing the air voids in concrete specimens. Additional parameters such as the spacing factor, air-void size distribution, and shape can also be extracted via a surface scan of the prepared specimen. Based on their study, Nambiar and Ramamurthy (*47*) concluded

that concrete specimens with a smaller size distribution of air voids exhibited higher strength. When a high amount of air entrainment was added to a specimen, bubbles tended to merge and form larger air voids. The result was a larger spread in the air-void size distribution, which decreased the strength of the concrete. Nambiar and Ramamurthy's results also indicated that the air-void shape did not have much influence on the strength and density of foam concrete.

In their image processing, Nambiar and Ramamurthy suggested five different morphological operations that are useful for image enhancement: dilation, erosion, opening, closing, and hole filling (*47*). Different combinations of these filters could be used to achieve the desired object isolation outcome. With these implementations, they were able to identify air voids and extract air-void parameters such as the total area, perimeter, and equivalent diameter of every defined air void in the specimen. These parameters could then be used to obtain statistical data such as the air-void percentage, air-void size distribution, pore shape, and spacing factors for each scanned specimen. An air-void volume was approximated by scaling the two-dimensional air voids into a third dimension.

## 2. EXPERIMENTAL SETUP AND METHOD

In light of the literature review, a typical ultrasound monitoring system (*30*) is shown schematically in Figure 2.1. Based on the above design, the current study adapted and developed various monitoring systems for two phases of study. Monitoring systems were built to test mortar and concrete, respectively, in these two phases of study.

### 2.1 Phase 1: Test Rig for Monitoring Mortar

Figure 2.2 shows the experimental setup for the current study, which was designed to measure the velocity of an ultrasonic pulse (or p-wave). As shown in Figs. 2.2a and 2.2b, the test rig was composed of three parts: two outside plates and one semi-circular internal block. These were all made of acrylic. There was a circular opening for the installation of transducers on either side of the outside plates. The ultrasound transducers were flush mounted at the inner surfaces of the plates. To protect the transducers, a thin film was applied to the inner surface of the sidewalls. The horizontal separation between the two transducers was 2.41 cm for the initial testing of mortars.

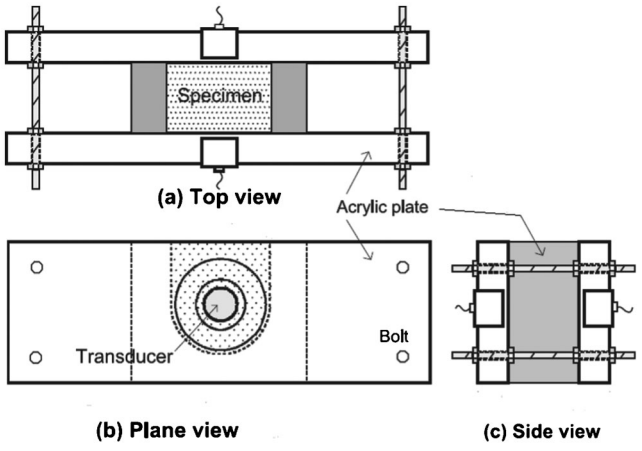


**Figure 2.1** Schematic diagram of typical ultrasound monitoring system (diagram taken from Lee et al. (*48*)).

A pair of Olympus Panametrics-NDT ultrasonic contact transducers (V101, with a resonance frequency of about 1 MHz) was used for both the source and receiver. An ultrasonic signal was sent from an Olympus Panametrics-NDT pulser-receiver (5077PR). The received signal was connected to a Tektronix digital oscilloscope (TDS2014B). The time-domain waveform was then stored for subsequent processing using standard MATLAB programs. Initially, the Tektronix TDS2014B was used for the data acquisition. A USB flash drive was attached to it and data were acquired manually every 5 min over the course of the first few hours. For long experiments, this approach is not feasible. In a later revision, the USB-VISA interface of the TDS2014B was configured to work with MATLAB's data acquisition toolbox. This allowed waveforms to be saved directly into MATLAB with minimal user intervention. It also enabled more waveforms to be saved each hour so that a high-resolution time-lapse movie could be generated.

### 2.2 Phase 2: Test Rig for Monitoring Concrete

Mortar was used in the initial tests prior to the use of concrete. Because concrete is a highly heterogeneous material, the presence of coarse aggregates caused a significant scattering effect for the ultrasonic tests using the 1-MHz transducer. It was found that the sound energy provided by the 1-MHz transducer was insufficient to transmit the ultrasound pulses through the 4"-thick concrete sample.

A 0.5-MHz transducer (type V101 with a resonance frequency of 0.5 MHz and diameter of 1") was used in the second set of experiments to measure the p-wave velocity of the sound transmitted through fresh concrete. The concrete used in these tests was composed of a mixture of cement, fine aggregates (size no. 30), coarse aggregates (size no. 8), and water. The test rig for the second set of experiments had an internal cross-sectional area of 4" by 5" and was built to hold a 4"-thick sample. The new test rig was designed to accommodate the largest coarse aggregates used in the ultrasound measurements, i.e., the thickness of the sample was at least 3 times the size of the largest aggregates. To minimize reflections from the edges of the test rig, an inner block was used instead of plexiglass. Figure 2.3 shows a photo of the test rig built for testing concrete.

For the 0.5-MHz transducer, subsequent experimental results suggested that the ultrasound signals (measured at the receiver) were not strong enough to

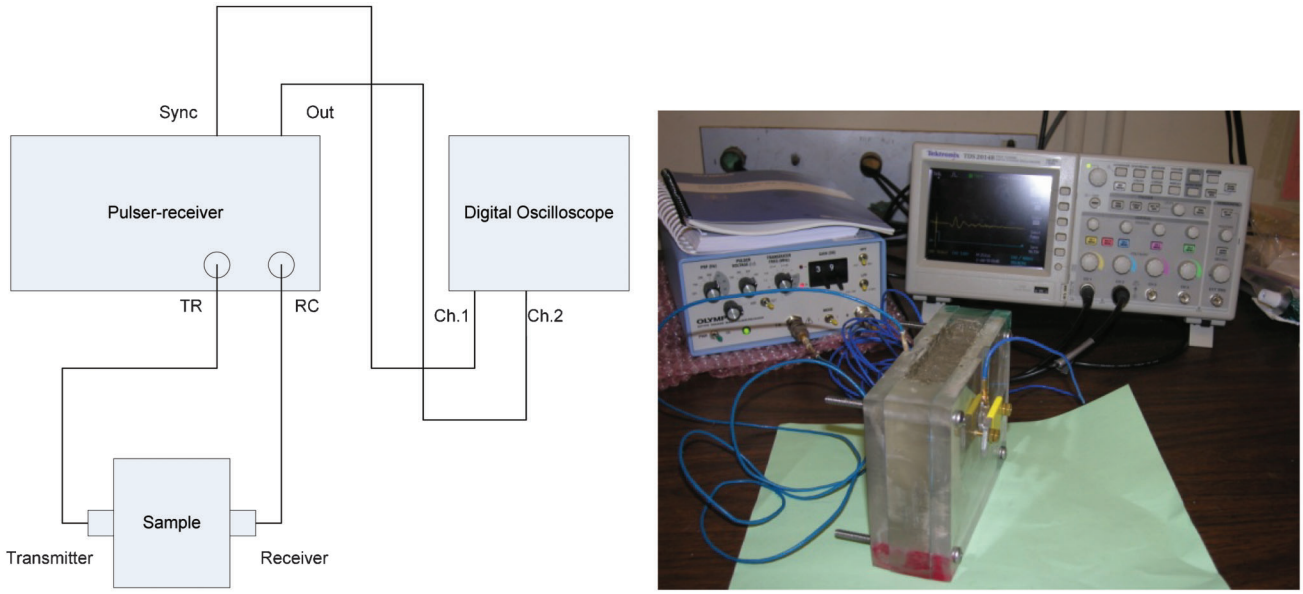


**Figure 2.2** (a) Block diagram and (b) photo of experimental setup for current study.

allow measurements within the initial 5-h hydration period. A further improvement was needed that could be achieved by using an ultrasound probe with lower resonant frequencies. This was because the attenuation of the sound pulses at lower frequencies was generally less than those at higher frequencies.

Because of these earlier experiments, a revised test rig was constructed to hold a 4"-thick concrete/cement specimen. To reduce the effect of multiple reflections from the bottom edges of the experimental rig, the inner plexiglass blocks were replaced with four 1"-thick rubber blocks.

Figure 2.4a shows the test rig. A pair of Ultran ultrasonic transducers (GRD140 and GRD200) was used for the measurements (see Figure 2.4b). The resonance frequencies of these two transducers were 140 kHz (GRD140) and 200 kHz (GRD200). The GRD140 transducer was used as a transmitter and the GRD200 was used as a receiver in the measurements. These two transducers provided more acoustic power, which allowed broadcast signals to be transmitted through the specimen during its setting stage.

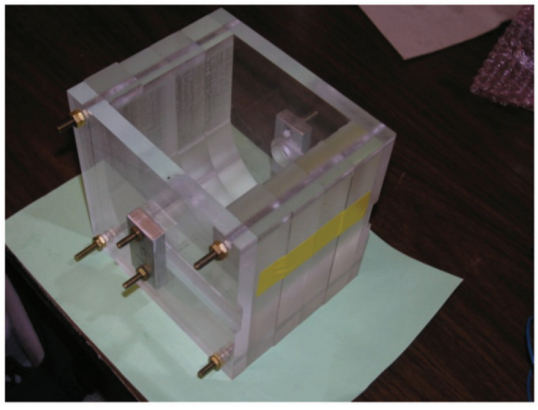

**Figure 2.3** New experimental test rig to hold 4"-thick concrete samples.

### 2.3 Development of Data Acquisition System

The data acquisition system went through several major revisions. The basic configuration is shown in Figure 2.2a. The synchronized output of the Panasonic NDT pulser-receiver (5077PR) corresponded to the reference time when the pulse was sent to the transmitter. The synchronized signal was a low-amplitude square wave with a pulse width corresponding to the excitation pulse frequency. The output terminal of the pulser/receiver was the measured signal, whose amplitude could be adjusted in increments of 1 dB up to a gain of +59 dB. This setting allowed small signals to be amplified prior to digitization.

Based on the time-domain signal analysis, it was realized that higher resolution noise sampling was needed to obtain a more precise location for the signal onset time. Because of the low vertical resolution of the Tektronix TDS2014B, the noise occupied 3 of the 256 bins available in an 8-bit digitizer. Because some of the triggering algorithms found in the literature (see Section 3 for details) required a full waveform to be analyzed, clipping the signal was not an option. A digital/analogue converter with a higher resolution was required to obtain a better representation of the noise without clipping the large signals. The transition to a 16-bit digitizer (National Instruments PCI-5922) allowed the noise to occupy many more bins, which


**Figure 2.4** (a) Revised test rig with rubber wall. (b) Ultran ultrasonic transducer.

made the noise averaging on the digitized data more reliable. A higher dynamic range (i.e., better resolution of small signals in the presence of larger signals) was achieved.

With the National Instruments PCI-5922, a LabVIEW control panel was developed because of the difficulty of interfacing the PCI card drivers with a newer version of MATLAB on a Windows 7 64-bit system. A highly interactive control panel was originally implemented, but it became increasingly difficult to manage because of the incompatibilities of certain modules with the newer version of LabVIEW. In the current implementation, LabVIEW's SignalExpress was used to set all of the desired data acquisition parameters in the background, as shown in Figure 2.5. The result was a much simpler interface, which allowed the user to select the file name and select when to start/stop the data acquisition. Data were stored in a LabVIEW container file format. Later, the experimental data were imported into MATLAB and converted into a more convenient matrix representation for subsequent analysis.

Originally, a 128-waveform average was performed automatically on the digital oscilloscope (TDS2014B) prior to outputting the results to a single waveform. Waveform averaging allows the suppression of random noise fluctuations. On the National Instruments PCI-5922, only one waveform was taken during each data acquisition interval. This was done intentionally to test the capabilities of the higher resolution digitizer and to analyze the noise characteristics via an FFT. The intention was to design a low-pass filter that would remove much of the high-frequency noise from the signal and output a smooth waveform. A triggering algorithm was used on the smoothed waveform for onset time determination. Further analysis was performed on the raw waveform to determine its spectral components.

## 2.4 Design of Test Rig–Specimen Container

Several different sets of ultrasonic transducers were tested in the present study: 1 MHz, 500 kHz, 350 kHz, 200 kHz, 140 kHz, and 100 kHz. In general, the lower frequency transducers tended to exhibit less attenuation. Therefore, transducers of the order of 100–350 kHz were selected for the more recent experiments on concrete. Different sensor mounting plates needed to be fabricated to accommodate the various ultrasonic sensors shown in Figure 2.6.

The basic design of the specimen container for the through-transmission experiments consisted of multiple thin sidewall panels (either rubber or plexiglass) clamped between two sensor plates (*4,29,30*). Initially, a 1"-thick plexiglass sidewall container was constructed to hold the specimen in earlier experiments. Multiple 1"-thick layers could be added to the specimen

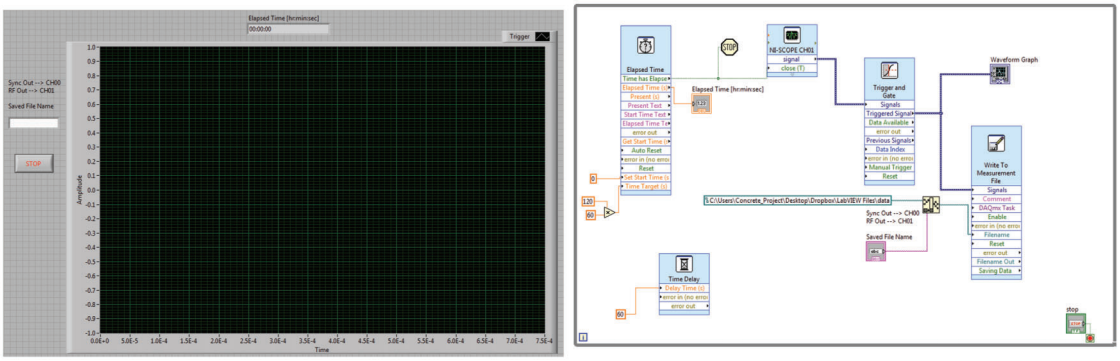

**Figure 2.5** LabVIEW control panel and wire diagram for National Instruments PCI-5922.

**Figure 2.6** Ultrasonic transducers used in present study: 1-MHz transducer (right), 500-kHz transducer (center), and 100-kHz transducer (left).

container to increase the sample thickness. Eventually, a rubber sidewall construction replaced the layered plexiglass design. The use of rubber sidewalls started with the 160-kHz test rig shown in Figure 2.4a. The original justification was that a U-shaped channel needed to be carved to avoid the possibility of interference effects from the sharp edges at the base of the specimen container. Rubber was much easier to remove once the specimens solidified in the test rig. The assumption was that rubber would dampen much of the structurally propagated ultrasonic signals and ensure that only the acoustical propagation path was measured in the experimental setup.

In a more recent revision of the experimental setup, the rubber-sided container was replaced by a rigid sidewall design with detachable sensor plates. One of the issues with the rubber-walled construction in the old test fixture was that the rubber deformed when clamped between the two sensor plates. This deformation gave rise to alignment and thickness variations between different test runs. The old test fixture design relied on coupling the ultrasonic transducers into a sensor plate that was fixed to the specimen container. When the top and bottom edges were compressed, the thickness difference could be up to 0.2". Compounded with the effects of using different sets of hand-drilled sensor plates, varying amounts of ultrasonic gel, and different sensor mounting depths, the total error in determining the actual signal path length became appreciable.

Alternatively, using the same pair of sensor plates across different sets of rigid specimen containers made misalignment less of a concern because the same amount of misalignment would be present in all of the trials. A rigid sidewall construction allowed higher tolerances to be achieved in sample thicknesses. Thus, the sample thickness also became a constant. A variable sample thickness is irrelevant in a P-wave velocity analysis as long as the sample thickness can be precisely quantified. For direct signal amplitude comparisons, it was desirable to keep the sample thicknesses constant. In the present study, a channel width of 4" was selected for the specimen container, which was about the same as the thickness of the old rubber-walled test setup. Figure 2.7 shows the revised specimen holder for the experiments.

## 2.5 Testing Procedures

Mortars were used for the initial tests. These mortar specimens contained 2.01 kg of cement, 844.2 ml of water, and 4.36 kg of natural sand. The *w*/*c* ratio was kept constant at 0.42. Varying amounts of AEAs were added to the water prior to mixing. The mixing procedures adhered to the ASTM standards. Fresh mixtures were placed in the test rig immediately after mixing, and the time-domain signal was recorded in increments of 5 min.

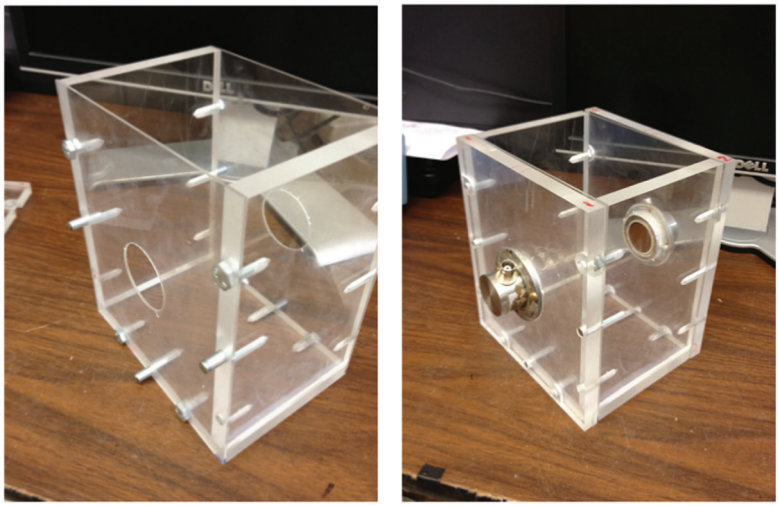


**Figure 2.7** Recently improved rigid sidewall test fixture consisting of (a) specimen container and (b) pair of detachable sensor plates aligned to specimen container by three metal pins.

The air content of the specimens was measured via two independent methods in addition to the ultrasonic measuring technique. The first method is known as the isopropyl-alcohol method (*49*). This method provided a rough estimate of the air content in fresh mortars, but it also relied on the skill of the operator. Because the measured results were rather inconsistent across the different tests conducted from one day to the next, this method was not used beyond the preliminary tests.

An alternative method for measuring the air content of a fresh mixture was based on the measurement of the weight of a standard unit (a 400-ml fresh mortar specimen). Three different layers of the test specimen were poured into a standard test cylinder. Each layer was tampered, and any excess mortar was removed from the topmost layer. The weight of the unit was measured, and the air content was calculated based on the known composition of the test specimen.

The time-domain signal was acquired using a digital oscilloscope (Tektronix TDS2014B or National Instruments PCI-5922). An onset time selection algorithm based on the energy density of the signal was applied to find the vicinity of the first onset. Then a zero-crossing search was used to identify the true onset time to improve the predictions.

After the specimens hardened (i.e., about 10 days after pouring), they were sliced and polished based on ASTM C457. Four to six layers of black ink were applied in an alternating cross-pattern to add contrast to the samples prior to scanning. The samples were darkened and corn starch was then applied to fill the air voids. The samples were scanned at a resolution of 3,175 dpi and processed using a MATLAB image processing routine developed specifically for the project.

## 3. DATA PROCESSING TECHNIQUES

### 3.1 Time-Domain Triggering Algorithm

Figure 3.1 shows a typical set of the through-transmission data of a time-history waveform for the ultrasound signals recorded at the receiver. Prior to the arrival of the transmitted pulse, only background noise was measured. After a certain time lag, the arrival of the ultrasound signal was evidenced, which was shown as an apparent increase in the amplitude of the measured ultrasound. Knowing the time lag, it was possible to determine the arrival time (or the onset time) of the measured signal. For a given specimen thickness, it was then possible to determine the velocity of the compressional wave, i.e., the p-wave of the ultrasound. The p-wave velocity was then used to correlate the air content of the cementitious specimens. Figure 3.1a shows typical results where the background noise was much lower than the ultrasound signal.

In this case, a crude algorithm based on the noise threshold was initially developed to determine the onset time of the measured signal. The average background noise level could be estimated from the measured waveform. The onset time was then determined as the time when the first peak of the measured signal exceeded the background noise level. Unfortunately, the background noise threshold did not work well in situations with low signal-to-noise ratios (SNRs), i.e., when the noise was comparable to the signal. As seen in Figure 3.1b, the onset time of the detected signal can potentially fall within a large region of ambiguity. It is apparent that an algorithm based on the background noise threshold may not be the best approach to determine the onset time.

A more sophisticated algorithm is needed to identify small trends within the leading edge of the signal to determine the onset time. An energy approach may yield more favorable detection rates. A review of several energy-based triggering algorithms can be found in Ref. (*50*). One of the most convenient methods can be summarized as follows.

The averaged accumulated energy of the measured signal is defined as:

$$\delta = \sum_{k=1}^{N} x_k^2 \Big/ \alpha N \tag{1}$$

Where $x_k$ is the amplitude of the discretized signal measured at the receiver, $N$ is the length of the

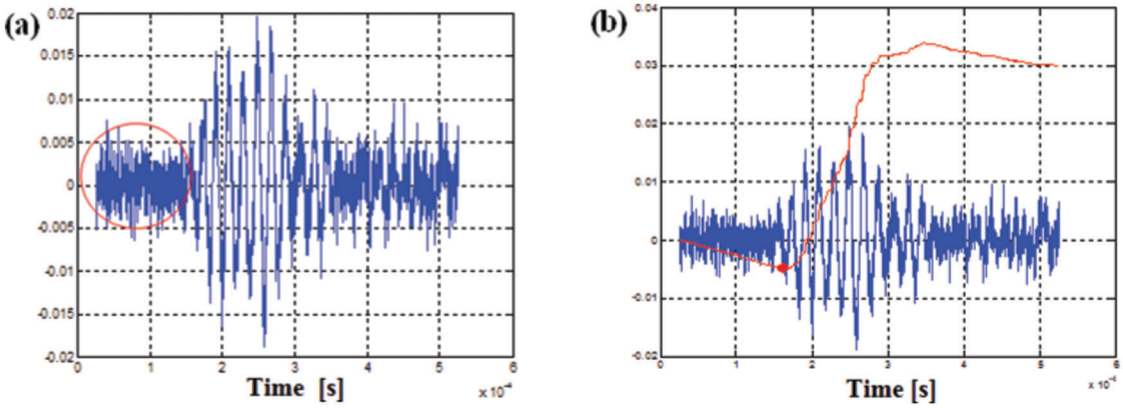


**Figure 3.1** Representative signal waveforms. (a) Background noise level was circled in red in the signal wave form. (b) The red line shows the numerical result for the detection of the onset time. The signal onset was determined by a triggering algorithm that distinguished the start of the signal from the background noise.

discretized signal, and $\alpha$ is an adjustable parameter. Based on the Hinkley criterion (*50*), a controlled parameter $\gamma_i$ can be defined as:

$$\gamma_i = \sum_{k=1}^{i} (x_k^2 - i\delta) \tag{2}$$

Figure 3.1b shows a plot of the time-history of the calculated $\gamma_i$ according to the Hinkley criterion. The onset time is then obtained by finding the global minimum, where there is a change in sign for $\gamma_i$. Based on a visual inspection of the time histories of the measured amplitudes of the ultrasound waves and $\gamma_i$, a trial and error approach is usually required to optimize the adjustable parameters $\alpha$ and $N$.

Figure 3.2 shows a set of typical results obtained via the Hinkley criterion. It is found that during the first 3 h, the sound speed is relatively constant at around 600 m/s. From 3 h to 8 h after the mixing, the sound speed increases sharply from roughly 600 m/s to about 1,800 m/s.

The implementation of the Hinkley criterion discussed above is contingent on a visual inspection and refinement of the adjustable parameters. Visual inspection is difficult when the measured signals have low SNRs. An improved method known as the Akaike information criterion (*50*) requires minimal user intervention. Nevertheless, a visual inspection is still required to confirm the calculated results because of the potential to detect false-positives. Initially, an algorithm based on the Hinkley criterion was implemented because of its simplicity. However, it was soon realized that the selection of the adjustable parameter was quite arbitrary and the results from a manual search tended to yield better results.

An alternative algorithm was developed in MATLAB to address some of the issues associated with the previous implementation of the Hinkley criterion. In the revised algorithm, the characteristics of the background noise from each individual waveform were analyzed. Recorded waveforms at approximate time intervals of 5 min were then stored for subsequent processing. The average of the background noise level was subtracted from the entire signal before the total signal energy was computed. This procedure was rather similar to the process described in Eq. (3.2) in the derivation of the Hinkley criterion. Instead of subtracting a negative trend from the results using a fitting parameter, a moving average filter was implemented.

The sensitivity of this moving average filter could be adjusted by setting the number of sample points to average over, along with the energy density needed to trigger the event. Setting the triggering threshold of the energy density to about half the peak energy level of the background noise tended to generate fewer false positive events. The filter allowed both positive and negative deviations from the mean to be detected because it was based on an energy approach. Figures 3.3a and 3.3b show a representative result for one waveform. There were typically 24 different waveforms to be analyzed in a 2-h experiment.

As shown in Figure 3.3b, a unique crossing can often be found within the vicinity of the area where the energy threshold intersects with the accumulated energy inside the boxcar filter. This intercept does not correspond to the actual onset time recorded. The onset time is taken to be the end-point of the boxcar where the threshold is triggered. Because the noise characteristics of the signal tend to be stationary, the

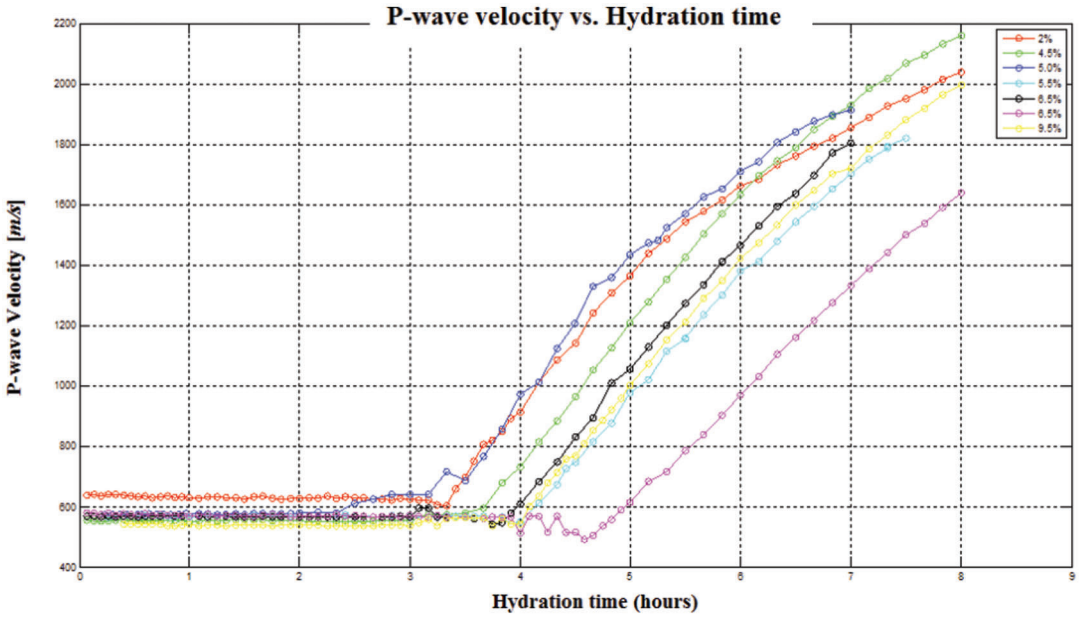


**Figure 3.2** Predicted P-wave velocity versus setting time for fresh mortar specimens with different air content. The onset time estimations are based on the Hinkley criterion. An air meter was used to estimate the percentages of air contents.

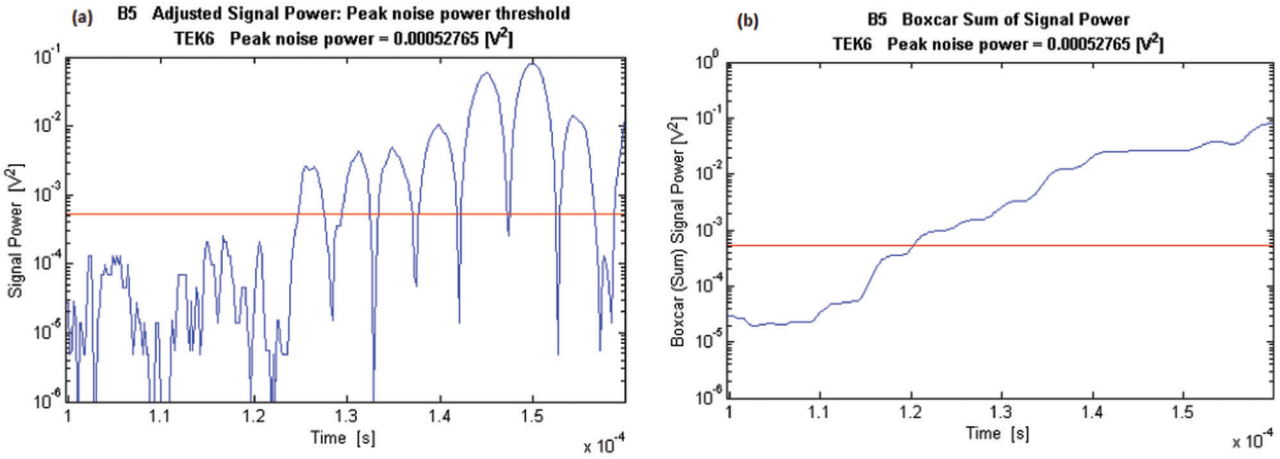


**Figure 3.3** Intermediate results for energy-based moving average triggering algorithm. (a) This plot shows the signal power after the mean noise has been deducted. (b) This plot shows the sum of the energy contained within the moving boxcar filter. The red line corresponds to the user-defined triggering threshold.

developed filter compares the energy density of the noise to the energy density of the signal over a finite time interval. This approach yields a more global set of parameters that can be applied to different samples within a given set with minimal user intervention. A normalized waveform approach has been attempted in the past; however, owing to the low SNR conditions, the noise gets scaled as well. This makes isolating the onset non-trivial.

Figure 3.4 shows the location of the triggered signal onset time on top of a series of waveforms taken during the 2-h experiment. Based on visual inspection, the arrival times appear to be almost identical across the various measurements taken. This visual trend is reinforced by the low variations in the detected onset times obtained from the triggering algorithm. The results shown in Figure 3.3 and Figure 3.4 were acquired using an 8-bit digitizer; the noise was limited to about 3 sampling bins, which may account for some of the spread in the detected onset times. The results from the 16-bit digitizer were not extensively processed because of concerns regarding the validity of the experimental data taken with the rubber-walled test rig. Instead, more emphasis was placed on improving

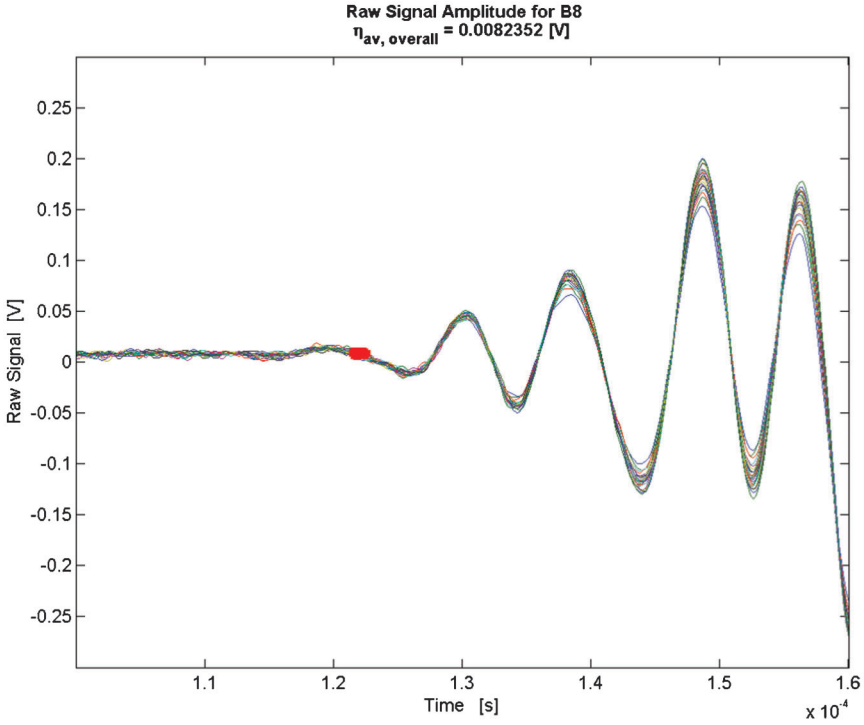


**Figure 3.4** Analysis of raw time-domain signal over two-hour period. Multiple waveforms (corresponding to 5-min time delays) are shown in the plot. The red dots indicate the detected onset time obtained from the developed triggering algorithm.

the experimental setup and developing image processing capabilities.

### 3.2 Image Processing Techniques

Several deficiencies were identified in the Bubble Counter (BC) script that was developed by Peterson et al. (*46,51*). In particular, the BC script assumes that the analyzed sample regions are perfect within a rectangular selection area. It also downsamples each high-resolution scanned image prior to processing and provides minimal visual feedback on what is being counted. Visual feedback is especially important in situations where samples are not sufficiently polished or contrasted.

The development of an alternative image processing routine that complies with the ASTM C457 standards was explored using MATLAB's image processing toolbox (IPT). This approach allows valuable time to be saved because minimal low level programming experience is required. With the MATLAB implementation, full resolution scanned images can be analyzed and individual bubble statistics can be extracted. A bubble is defined as a set of connected elements. This means that overlapping bubbles tend to be counted as a single bubble. A watershed algorithm can be applied to estimate the boundaries of overlapping bubbles to decompose large bubbles into several smaller segments. Additionally, high-performance computing methods can be implemented to decompose a large image file into a series of smaller, overlapping strips that can be processed simultaneously. These efficient computing approaches are necessary when high-resolution images are processed on a system with limited memory.

Optical characterization of the air content provides a more consistent, reproducible result than any of the other previously discussed methods for predicting the air content of cementitious specimens. Once the specimens have been scanned, various image processing techniques can be applied retroactively. The major drawback of optical characterization is that the samples need to be hardened thoroughly prior to slicing. Typically, this process can take a few days or weeks, depending on the size of the test specimens. After slicing the samples, the specimens can be contrasted and scanned based on the relevant ASTM standards.

In the initial procedures, multiple layers of ink were applied in a grid pattern of parallel lines (within each layer); then, the pattern was offset perpendicularly between adjacent overlapping layers. Once the ink dried, a layer of corn starch was compacted on top of the specimens and excess powder was removed. This approach allowed the air voids to be colored white, and distinguished the indentations on the sample from the dark background. Corn starch was selected based on its small particle size and bright white appearance. Previously, barium sulphate was used as an optical contrast agent in other studies.

The prepared specimens were scanned at a resolution of 3,175 dpi using a high-resolution HP photo scanner without any other filters applied. The samples were scanned as 8-bit gray-scale images. Later, a resolution of 3,600 dpi was adopted because it is one of the hardware-supported settings. This setting ensured that minimal scaling artifacts were present when the full resolution image was analyzed on the computer.

#### *3.2.1 Mortar Specimen Characterization Techniques*

Initially, only mortar specimens were tested. An analysis of these mortar specimens provided a basis for comparison between the BC script and MATLAB IPT algorithm implementations. Additional technical capabilities were introduced in the development of the IPT algorithm. The most prominent features are as follows: (1) analysis of the full resolution scanned image, (2) selective removal of surface defects via a non-rectangular sampling area, and (3) quantification of bubble statistics.

The analysis of a full resolution image allows bubble shapes to be identified, and it provides a more representative sampling of the physical specimen. It also provides a visual feedback system that corresponds to the actual sample being analyzed. The binary image obtained from the image analysis algorithm represents each detected air-void pixel as a white dot, whereas everything else is black. Ideally, the contrast between the white powder (corn starch) and black background should be large to yield the least number of false positives in the air-void detection. The bubble detection section of the IPT algorithm relies on identifying a threshold value that maximizes the number of bubbles detected while minimizing false-positive detections. The calibration of the thresholds can be performed visually by overlaying the binary image on top of the original contrasted image and comparing the two results until a suitable agreement is achieved.

There are several mechanisms for the false positive detection of air voids. Some of these issues are not apparent based on the BC script because no universally accepted standards are provided. In certain cases, a large region of air voids can be detected in poorly polished samples. Often, a simple change in the detection threshold can remove this effect, but there is a risk that poorly contrasted air voids would not be detected elsewhere in the sample. Another set of mechanisms for false positive detection is the result of contamination by the white powder.

The white contrast powder can contaminate the scanned results in multiple ways: (1) powder falling out of the air voids when a contrasted specimen is flipped and placed face down on the flatbed scanner, (2) powder streaking caused by moving the sample to reposition it on the scanning surface, and (3) powder mixing with the ink particles during the compacting or excess powder removal phase. Although careful preparation and processing procedures were used, these mechanisms could not be eliminated entirely because of the inherent material properties of corn starch and the pigments used in the ink. Modifications to the scanning

procedures to address these issues will be detailed in a later section. In the initial IPT algorithm, these defect regions were eliminated via a digital masking layer.

Defects (e.g., uneven polishing, powder streaks, air entrapment voids, etc.) were systematically removed via a digital masking layer. This approach allowed undesired sampling regions to be removed prior to the counting of air voids. The implementation of the algorithm relied on the creation of two separate layers for the scanned sample. The first layer was the original scanned image. The second layer was a defect mask that was generated by overlaying a transparent image on top of the first layer. To isolate undesired regions on the scanned test specimen, a digital paintbrush was used to color these regions black. A transparent layer allowed the user to view the image underneath while manipulating an entirely different image. Anything exposed through the transparent masking layer was analyzed in the bubble counting analysis. In converting the black and transparent images to a binary image, the transparent regions needed to be colored white. The two layer images were saved as separate files.

Figure 3.5 shows the processing technique used on a typical mortar specimen. Here, the sample was poorly polished along the upper right edge. A corresponding defect mask was generated to remove this region from the analysis window. The sampling area was maximized by following the contours of the test specimen. The threshold value was set to 150 (out of a maximum of 255) because of the high white levels achieved in the sample preparation process. If the white powder indicator was severely contaminated by the black ink particles during sample preparation, a much lower threshold value had to be applied.

With the proposed approach, the sampling area could be maximized because it was no longer limited to a rectangular region. For example, a circular aperture could be exposed by the masking layer in the analysis of the circular cross-section of the test specimens. Typically, an approximately one-centimeter region

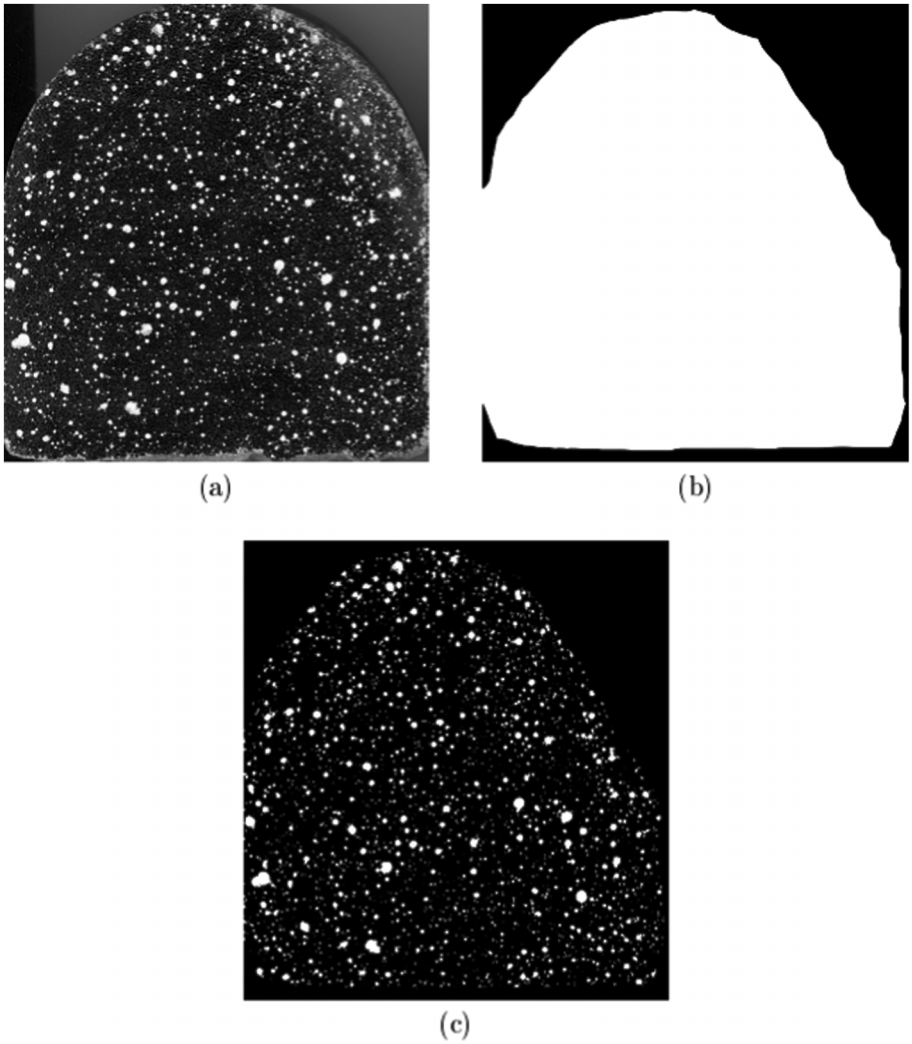


**Figure 3.5** Mortar specimen image processing techniques. (a) Contrasted image with polishing defects. (b) A defect mask is created to remove both edge defects and polishing defects. (c) The binary bubble detection image generated by the IPT algorithm.

around the edge of the physical sample is discarded to avoid analyzing the effects of the specimen container.

After the sampling region was defined, the IPT algorithm combined the masking layer with the original image. The masking layer was analyzed to compute the exposed area. The original image was analyzed, and a binary image was constructed that only displayed the detected bubbles. Afterward, the masking layer and binary image layer were combined. Anything that was not exposed by the masking layer was discarded (i.e., set to black). Now, the composite image could be counted; each white pixel contributed a value of 1 to the pixel-by-pixel bubble count. Because the actual image information was stored in a 2-D matrix representation, performing a double array summation yielded the total number of air-void pixels. This value was averaged over the total exposed area of the masking layer. The end result was an air content percentage, which was weighted against a non-rectangular sampling region.

When using the BC script, voids due to air entrapment needed to be colored black prior to running the program. Because of the small sample surface area, excluding these defect regions was often unavoidable. Whenever air entrapment voids were encountered by the BC script, they were registered as a pure black region because of the selective treatment process described above. The area occupied by these defects was already included in the total sampling area. Thus, when the BC script encountered these regions, it treated them as if they were devoid of any air content. This led to a slight under-prediction of the total air content.

When the defect area represented a large portion of the sampling area, the sample had to be discarded because of poor sample preparation. However, for intermediate cases where such regions needed to be included in the analysis window (because of the restrictions imposed on having a minimum selection area), an alternative exposed area weighting might have been more desirable. Adding a defect masking layer allowed the surface area occupied by the air entrapment voids (among other defects) to be removed entirely. This feature allowed more accurate computation of the air content in the presence of defects.

By using MATLAB's IPT functions to identify connected components (or bubbles), each individual bubble was automatically stored as a separate entry within a structured array. Bubble statistics such as the size and centroid locations were also computed automatically. Using this information, the bubble size distribution could be sorted into various size bins and then plotted. A polynomial curve fit was applied to the results to provide a qualitative graphical representation of the overall trends.

### *3.2.2 Bubble Size Distribution Histogram*

The output of the connected element analysis done in MATLAB's IPT contained the number of classified pixels in each bubble. This information was sorted into various size bins. Then, the number of occurrences were tallied and plotted on a log-log scale. Figure 3.6 shows the binning of the various bubbles detected by the

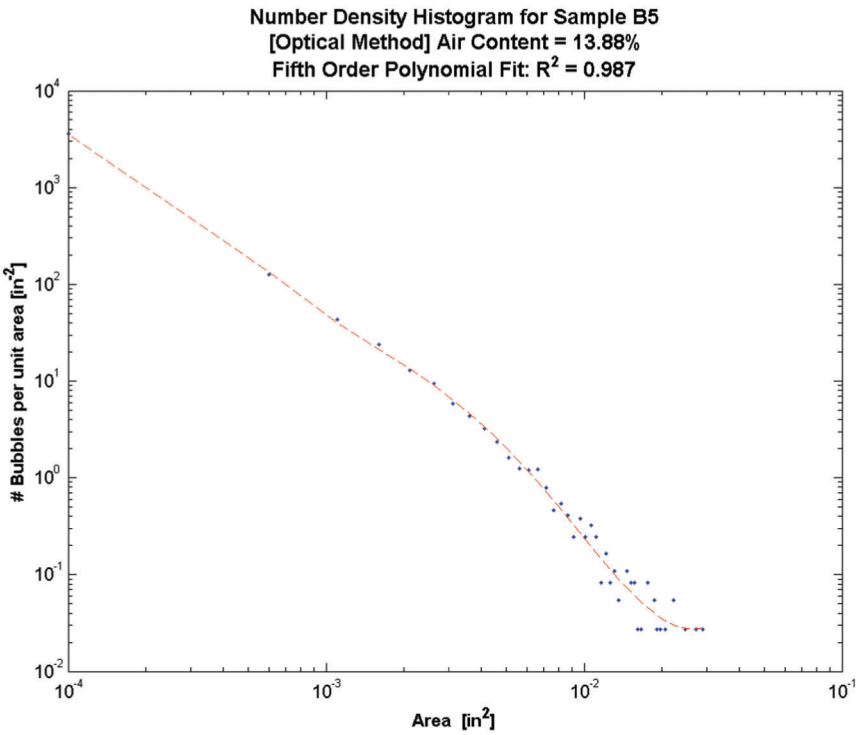


**Figure 3.6** Bubble size distribution histogram for one sample.

developed IPT algorithm. The surface area occupied by any individual bubble was computed based on the resolution of the scan and the number of pixels found in the connected element analysis. No watershed algorithm was applied to segment the bubbles into smaller components.

The ordinate in Figure 3.6 was normalized to represent a number density. This number density indicates how many bubbles of a particular size may be observed in a representative 1" square region. It was obtained by dividing the number of bubbles in a particular size bin by the total exposed sampling area. This allowed the direct comparison of samples with different areas on a common plot. For specimens consisting of multiple slices, the binned statistics were combined and the total effective area was used in the normalization. Then, a fifth-order polynomial was fitted to the data to infer qualitative trends. The fitted curves were plotted on a common figure to estimate the variations in the bubble size distributions between the different samples analyzed. Qualitative trends can be extracted from these simplified curves.

### *3.2.3 Coarse Aggregate Characterization Techniques*

The processing technique for coarse aggregate specimens was similar to the gray-scale image processing techniques applied to mortar specimens. The only change was the selective removal of the interior region of a coarse aggregate specimen prior to counting the bubble statistics. Typically, the interior region of the coarse aggregate was colored in by hand prior to scanning. Then, the BC script was used to analyze the resulting image. Coarse aggregate identification could be time consuming, and some degree of bias was introduced by the user in determining which regions to fill. Many times, it was difficult to differentiate the grain boundaries of the coarse aggregate from the mortar after the sample was inked.

Because of the powder contamination issues, filling in the interior region of the aggregate could be more effective if performed digitally on a computer. One approach would be to not fill in the aggregate by visual inspection of the physical specimen, but to do so on the digital image instead. The detected bubble map was overlaid on top of the contrasted scanned image to help the user identify pertinent regions to exclude from the count. The process is shown in Figure 3.7. The user was required to identify the aggregate grain boundaries and fill in the interior air voids (i.e., the green spots) after the image was processed in the first pass. A second pass was performed on the edited image to ensure that more accurate results were obtained.

A similar approach may be suggested as follows. Most of the aggregate identification could be performed by a visual inspection of the physical specimen. This could then be supplemented by digital manipulations of the smaller aggregate regions or defect regions on the computer. In either case, a large amount of user intervention may be required because of the loss of grain boundary definition after the samples have been inked.

No automated detection threshold selector was implemented as a proof of concept algorithm. Instead, it was left to the user to visually compare the overlap between the original image and a bubble detection overlay in order to refine the threshold levels. Figure 3.8 shows a representation of this process. Setting a low threshold tended to result in large numbers of false positives, which led to an overestimation of the air content. Setting too high a threshold led to underestimates, especially in situations where the edges of the contrasted images were not well defined. Because of slight variations between different contrasted samples, the threshold selection process should be performed on a sample-by-sample basis, as indicated in the literature.

For the developed IPT algorithm, it was often useful to look at the air voids located in the vicinity of the boundary that were partially below the masking layer. Based on a visual inspection of a 100% cropped image, the threshold level could be iterated in small increments in such a way that the detected bubble boundaries corresponded to the user perceived boundaries. For processing large numbers of samples, this approach may not be ideal. An automated threshold level selection algorithm should be implemented in the future.

### *3.2.4 Coarse Aggregate Edge Enhancements*

Several different approaches were investigated to identify a technique that could aid users in identifying the coarse aggregate grain boundaries more easily. The desired outcome was to have a semi-automated classification system for isolating the coarse aggregate grains. A common technique for this type of classification system is based on edge detection algorithms. The sensitivity of the edge detection algorithm needs to be tuned to detect only the edges present between the aggregate grains and paste. Based on the available built-in algorithms in MATLAB's IPT for edge detection, the Canny edge detection algorithm was selected for its ability to detect fine edge details.

Edge detection needed to be applied to an uncontrasted scanned image to obtain usable outputs. The image needed to be converted into grayscale prior to the application of edge detection filter. In addition, the image being processed did not need to have a high resolution because it was intended for large aggregate boundary identification. Unfortunately, the edges between the coarse aggregate in the specimens tested were quite similar to the surrounding mortar. This meant that the edge detection sensitivity needed to be increased to identify more enclosed objects.

Increased edge detection sensitivity can result in the detection of sand grain boundaries in a cement mix. One approach around this issue is to downsample the high-resolution image to avoid detecting the sand grain boundaries. Another solution would be to use the

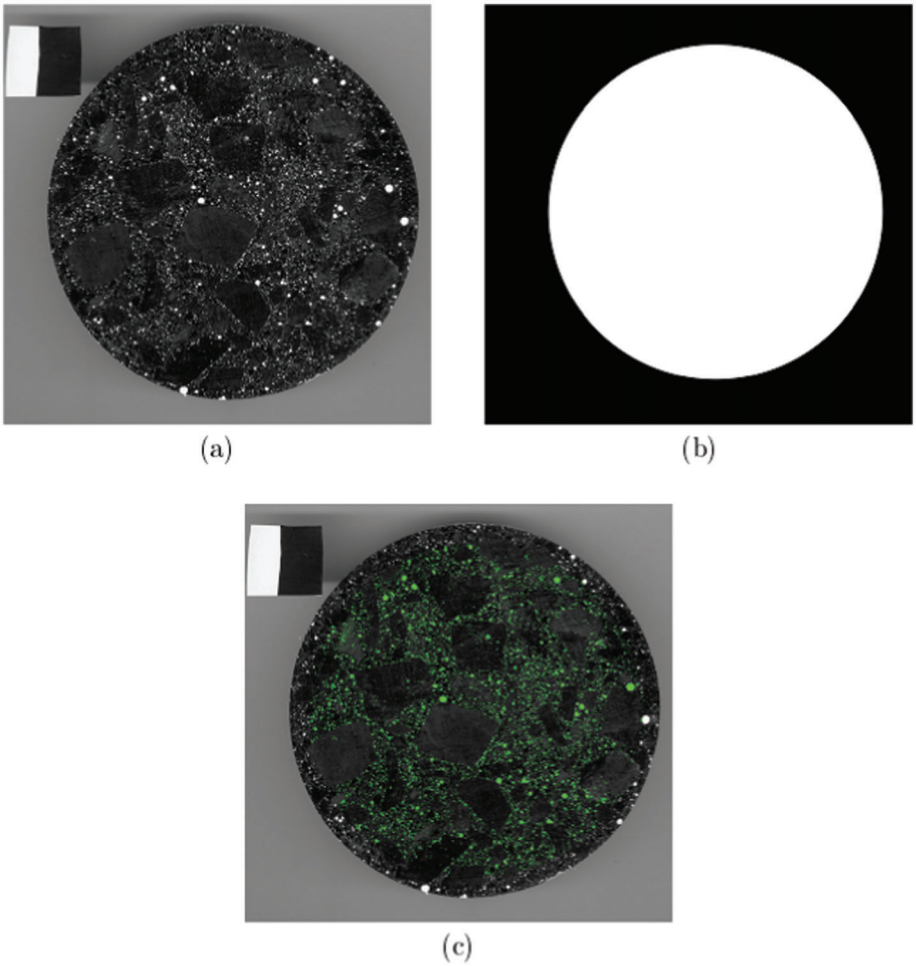


**Figure 3.7** Coarse aggregate processing technique applied to circular test specimen. (a) Contrasted scanned image, (b) digital masking layer, and (c) composite image with bubble detection overlay (indicated in green).

existing image and design a filter that only picks up grain boundaries that are larger than the characteristic spacing between the sand particles in the mortar. The advantage of this approach is that the grain boundaries for irregularly shaped coarse aggregate islands can be resolved almost exactly. Visual inspection of the specimens showed that many bubbles tended to nucleate near the boundaries of the coarse aggregate grains. Being able to clearly define these regions for aggregate isolation would increase the accuracy of the bubble count.

The edge enhancement technique was applied to grayscale images by taking two separate scans of the sample. The first scan was the uncontrasted image, which was used in the edge detection algorithm. The second scan was the inked sample that was coated with white powder and used in the bubble detection algorithm. These two images had to be scaled and aligned because they represented two different scans at potentially different resolutions.

Initially, a glyph was used as an alignment artifact in the two separate scans. This was later improved by noting that the edge-detected grain boundaries would serve as a better alignment indicator when a small section was left uncontrasted. This process is shown in Figure 3.9. This method improved the visibility of the underlying grain boundaries and helped the user in the aggregate identification process. The alignment process could be accomplished either manually using photo editing software or with the aid of the image registration tools available in MATLAB. However, an exact alignment cannot be guaranteed—especially when two different resolution images are scaled to a common size. A color image processing technique may bypass the alignment step altogether.

### *3.2.5 Color Image Processing Techniques*

Color image processing techniques for air-void detection were also considered. Much of the optical information was discarded during the gray-scale image conversion process. By using a colored image, more relevant information could be obtained for classification purposes. The primary colors detected by the photo-sensors on the scanner and those used in MATLAB were red, green, and blue. Hence, these

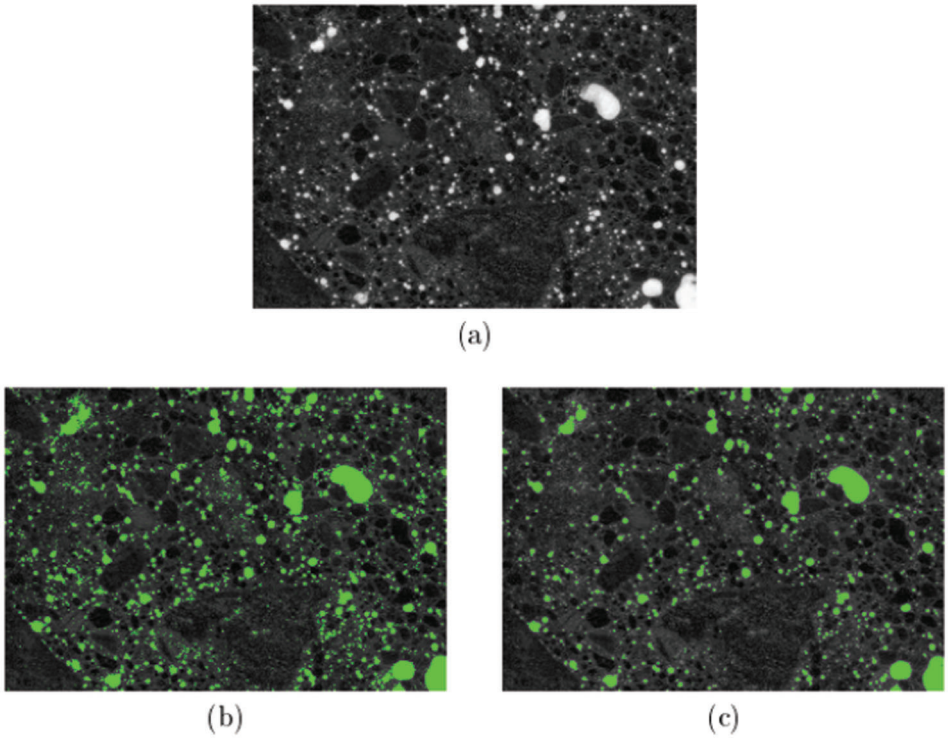


**Figure 3.8** Detection threshold selection process. (a) Original contrasted image. (b) Detection threshold set to 80. (c) Detection threshold set to 120.

same colors were selected as potential contrast agents. To reduce the number of false positives, several different color indicators could be selected to contrast the test specimens, depending on pre-existing background colors. A color indicator strip could be attached to the uncontrasted sample (either digitally or physically) to determine which color indicator would work best.

Peterson et al. (*46,51*) also considered a color processing technique in an unpublished paper. However, their technique was not the one implemented in the BC script. In their approach, a scan of the original specimen was taken. Then, the cement paste was stained a pink color and scanned a second time. The third scan was of the blackened and powdered sample. These images were aligned on top of one another, and individual layers of the image could be analyzed separately to perform image classification.

For example, the layer containing the stained paste could be used to identify regions of paste in the flattened image. The assumption was that the staining agent did not react with the coarse aggregate in the specimen. The air voids could be detected as done previously in the grayscale processing section. A set of 20 reference points were used to align different layers in the composite image, which were all taken at the same high resolution. Using the composite image and performing a color analysis combined with a principal component transform, the image could be classified based on the statistics of the intensity levels of the population of pixels defined as paste, aggregate, and/or air void. This technique did not work perfectly because of the transparency of polished quartz sand particles, which resulted in the region being detected as paste. There were also various issues associated with the misclassification of objects. However, the ideas presented appear to be reasonable.

An alternative color image processing technique was proposed in the current project using more recent developments in image processing techniques. Typically, an 8-bit color image was scanned at a resolution of 2,400 dpi. A finger paint and corn starch mixture was used to form a colored paste that was also water soluble. The primary attributes of the selection process were the ease of use and low toxicity. Samples were prepared by applying the paste to the top of a newly polished specimen. A plastic card was used to spread and compact the colored paste into the air voids. Then, the sample was rinsed in water and air-dried. Because of the expansion of the hydrated paste, residue was present in the dried specimens (especially near the edges of large air voids). A final wipe was performed with a damp cloth to remove the edge artifacts. The sample could then be scanned.

There is a possibility that only one high-resolution scan will be needed with this proposed technique. This assumes that there are no false positives in the uncontrasted sample. A more refined approach would involve two scanned images. The first scan would be used to identify false positive regions on the uncontrasted samples. The second scan on the contrasted sample would be used for air-void detection.

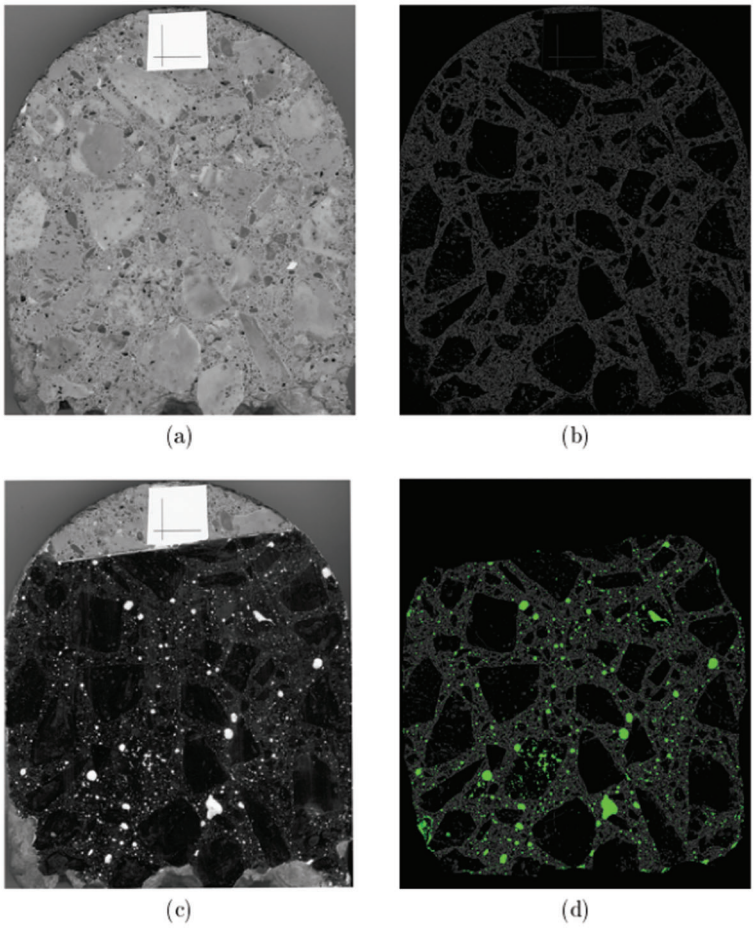


**Figure 3.9** Grayscale image processing technique using two separate image scans. (a) The original uncontrasted image. (b) The edge-enhanced binary image obtained from the original scan. (c) The contrasted image for air-void detection. (d) The composite image obtained by aligning the binary bubble detection layer with the edge-enhanced image. A defect mask was applied to isolate the region of interest prior to quantifying the air content.

Overlapping these two images and comparing the outputs would enable false positive bubbles to be detected and selectively removed via image subtraction. Figure 3.10 shows the application of a red colored paste to a typical coarse aggregate specimen.

The colored image was represented by a three-dimensional matrix in MATLAB. The layers of this matrix corresponded to the three principal colors: red, green, and blue. By taking the red color channel and subtracting one half of each of the remaining color channels, a filtered image was obtained. This filtered image corresponded to only the red color channel. A thresholding algorithm was applied to suppress the background levels that might have been present in the test specimen. Then, the detected bubbles were colored green for ease of visual inspection in later processing steps.

The highlighted circular region in Figure 3.10 shows an example of a false positive detection. In this particular example, the color indicator closely matched a background component. To overcome this issue, a deeper shade of red indicator would be necessary. Then, the detection threshold for the red channel could be raised in such a way that the light red aggregate would no longer trigger the bubble detection filter. The edge-detected overlay is also shown in Figure 3.10b. The combined result is a three-color image that represents the presence of grain boundaries and the locations of air voids. With the color contrast, the coarse aggregate grain boundaries become highly visible. Processing the physical sample and covering the red patches with black ink also becomes more manageable. The preference is left to the user at this stage.

Note that the cracks that developed inside the large air voids could be removed via image processing as long as the outer boundary encloses almost the entire crack. This filling operation has already been performed on the images shown above. Because the interior region of the aggregate is non-uniform, the edge-detected image only gives a rough indication of the grain boundaries. The user still needs to make sense of the image during the selective removal of porous aggregate grains. Further processing is required to isolate the coarse aggregate regions in a more automated manner.

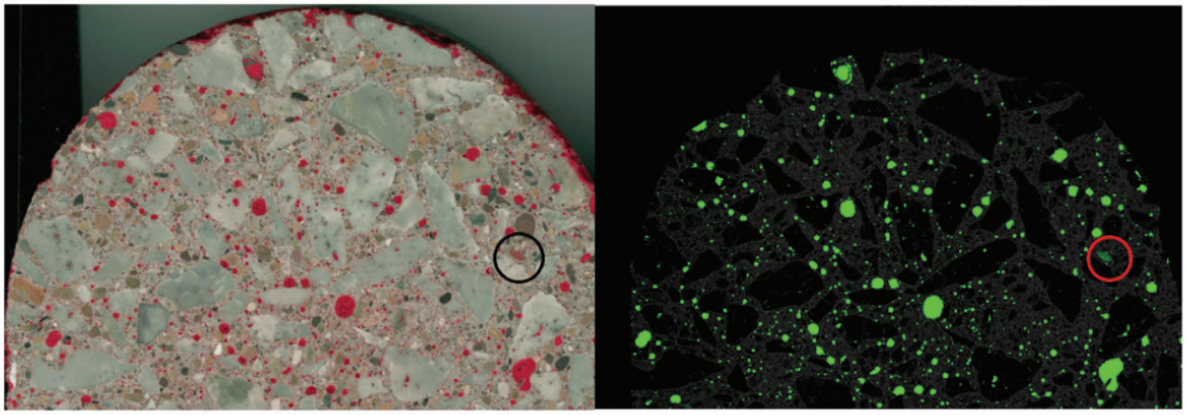


**Figure 3.10** Coarse aggregate grains. (a) Color-contrasted sample obtained by using red paste to fill air voids. (b) Composite image with edge-enhanced and bubble-detection overlays. The circled regions highlight a false positive detection event where the colored aggregate level exceeded the detection threshold set by the user.

### *3.2.6 Coarse Aggregate Detection Filter*

Once the coarse aggregate grain boundaries can be identified precisely, a digital filter can be applied to remove the interior region of the aggregate via a filling operation. This approach allows entire aggregate regions to be classified based on the outermost boundaries. The information obtained by the proposed filter can then be used to selectively remove bubbles within the interior region of the aggregate grains in the original scanned image. Classification would also enable aggregate statistics such as size and distribution to be analyzed.

To perform the classification, a color-contrasted sample was used. A grayscale image could also be used, but additional image processing steps would be required. Each processing technique has its own merits. For example, the grayscale processing techniques allow background levels to be suppressed by coating the entire sample surface with black ink. However, two high-resolution scans are required, which would almost double the processing time. Additionally, the two images would need to be aligned almost exactly to avoid the undesired deletion of bubbles along the coarse aggregate boundaries.

The color image processing technique may only require one high-resolution scan, which would make alignment unnecessary. However, the background levels in the sample would need to be suppressed to avoid false positive detection. Depending on which mechanism contributes to the largest amount of error in estimating the air content, one approach could be more favorable than the other.

Visual inspection could be used to identify many of the coarse aggregate grains in the (downsampled) images shown in Figure 3.10. This is because aggregate grains tend to have more uniform interiors than the surrounding mortar. The edge detection algorithm has sufficient sensitivity (when applied to a high-resolution image scanned at 2,400 dpi) to detect these small variations. Ideally, there should be a sharp contrast between the coarse aggregate grains and the surrounding mortar. One approach to achieve the desired contrast would be to select an aggregate that has a different color than the mortar. Another approach would be to dye the cement or use a colored mortar mixture. Based on the availability of the material and the standard concrete specimen composition, these avenues were not explored.

With the existing specimens, a filter based on the density of the detected edges seemed to be more relevant in isolating distinct coarse aggregate regions. The edge-detected binary image quantified the edge as a single pixel. By traversing the edge-detected image using a thicker structuring element consisting of a much wider brush stroke, small grains of sand could be removed. The structuring element selected was a circular disk with a radius of 10 pixels, corresponding to a scanned image at 2,400 dpi. This step ensured that small gaps of the order of the disk diameter were bridged to form enclosed objects for the connected element analysis (i.e., bubble detection).

The high-resolution image could be broken into long vertical strips with an overlap region of 1 pixel along each interior interface. The Canny edge detection algorithm in MATLAB was designed to produce no output for the 1 pixel border around the input image segments because of its gradient estimation subroutine. This domain decomposition process allowed the edge detection to be performed on each computational strip independently, and ensured that every interior edge was connected.

Edge detection is not bounded by CPU performance, but it can become memory intensive when large image files are processed. Decomposing the image into distinct blocks for processing allows the computations to be performed one strip at a time. For computer systems with higher memory capacities (>10 GB), a parallelized

algorithm could be applied to perform the edge detection for all image strips simultaneously. The edge-detected strips were stitched together along the common overlapping interfaces after the edges were identified. This produced a continuous edge along the interior region of the full-sized original image. The processing technique described is quite common in high-performance computing applications.

Next, small enclosed objects were removed from the binary image by setting a size threshold. For ease of representation, small aggregate regions were also removed so that only large aggregate regions were shown in the output image. Intermediate outputs from the filter are shown in Figure 3.11. In addition, regions enclosed within the coarse aggregate grains were removed via a filling operation in MATLAB's IPT. Note that the results shown in Figure 3.11c could also include large bubbles that are not enclosed inside the aggregate grain boundaries. A separate processing step was required to subtract these external bubbles from the coarse aggregate identification image. Once these steps were performed, the resulting image could be used as a digital mask to selectively remove the air voids enclosed by the aggregate grains.

In its current form, there are still some technical issues in the filter design. For example, closely spaced aggregate grains can potentially be counted as a single large aggregate region when large structuring elements are used to bridge the gaps in an edge-detected image to form the connected elements. In aggregate regions where there are densely clustered internal edges, the algorithm will not be able to identify the relevant grain boundaries with high levels of accuracy. More information would be required to isolate the missing outputs. Perhaps downsampling the image prior to performing the edge analysis will yield better results because most of the fine edge variations are discarded in the low-resolution image representation.

An approach that combines both high-resolution and low-resolution edge detection methods would ensure that most of the aggregate grain boundaries could be accurately identified. Additionally, it might be possible to incorporate the color of the mortar into a classification system because mortar exists in a narrow range of color values. By using more information obtained from color scans, a more detailed classification system could be constructed. This system might be able to differentiate the mortar, air voids, and aggregate within the specimens once implemented. However, the classification of mortar has not yet been explored in the current study.

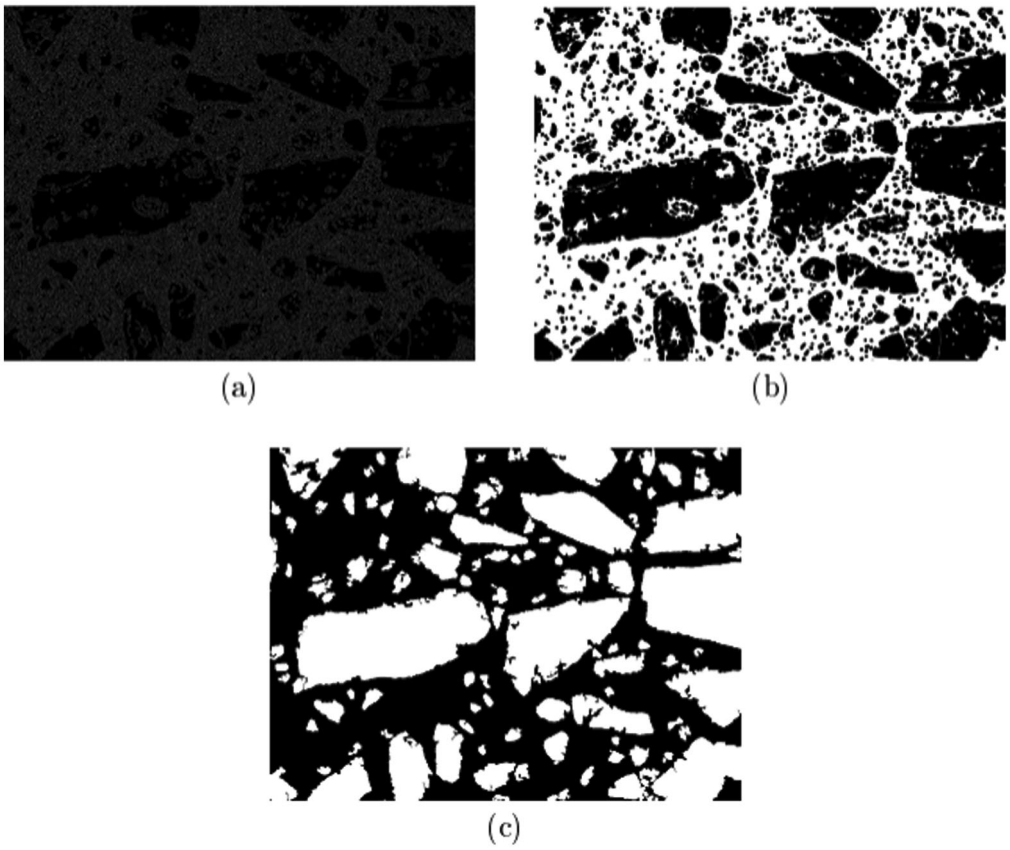


**Figure 3.11** Coarse aggregate identification filter. (a) Edge-detected image. (b) Structured edge-enhanced image. (c) Intermediate output of the filter, which includes aggregate regions and non-enclosed air voids.

## 4. MEASUREMENT RESULTS AND DISCUSSIONS

The main objective of the present study was to establish the feasibility of obtaining time-domain data within the first few hours of hydration for a 4"-thick fresh concrete specimen. An equally important issue for the project was the development of image processing techniques for examining hardened cementitious materials. Both techniques are essential for air-void detection, aggregate characterization, and the confirmation of the experimental results based on ultrasound measurements.

For the purpose of the current investigation, we were primarily interested in ultrasonic characterization that could be accomplished within the first two hours of hydration for typical concrete specimens. A minimum sample thickness of about 4" was predetermined to allow a more representative sampling of course aggregate specimens.

### 4.1 Ultrasonic Characterization of Mortar in Its Early Hours of Hydration

Longer hydration times tend to generate better quality signals because of the acoustic propagation of ultrasonic waves traveling through a more homogenized medium as the specimen hardens. More scattering of the acoustic waves is expected at the interface of heterogeneous materials (i.e., solid sand/aggregate grains and cement paste) during the first few hours of hydration. This effect is controlled by how much of each of the composite materials is present in the fresh concrete. Another scattering mechanism is the interaction between the air voids and the surrounding cement paste as an ultrasonic wave is experienced.

To test the transmission of ultrasound through cementitious materials, preliminary experiments were conducted by analyzing the specimens within the first ten hours. Because fresh concrete is a highly heterogeneous material (which usually consists of a mixture of cement, fine aggregates, coarse aggregates, and water), it was expected that the large size of the coarse aggregates (of the order of 40 mm) could cause significant scattering of the ultrasound. Therefore, cement (252 g) was mixed with water (120 g) and the fine aggregates (688 g) in the initial experiments. To minimize the effect of the non-uniformity of the fine aggregates, silica sand was used in the first set of measurements. Natural sand was then used as the fine aggregates for the mortar in the next set of measurements. The next two sets of experiments involved the addition of an AEA (0.2 ml) to mortars with the same composition.

Figure 4.1 shows the p-wave velocities of the setting silica sand mortars with (blue stars) and without air voids (red star). The measured results for natural sand mortars with (red circle) and without (blue star) air voids are also shown in Figure 4.1. In each set of data, a minimum of three separate measurements were conducted. Based on the measured data, several observations can be offered as follows:

- After mixing fresh mortars, the p-wave velocities in the setting mortars could be categorized into three regimes as time elapses:
  - The first regime has a constant p-wave velocity (about 450 m/s).

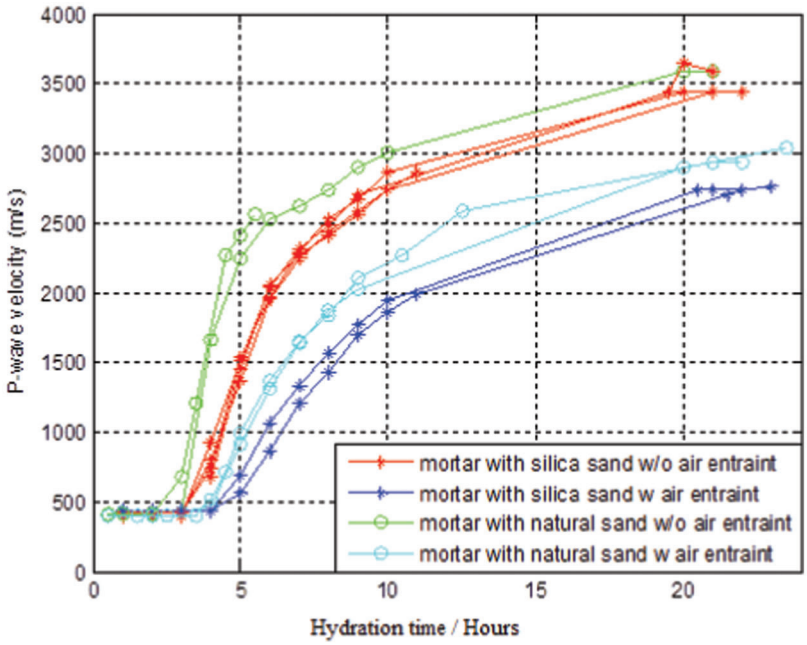


**Figure 4.1** Comparison of p-wave velocity versus hydration time (measured in hours) for different types of mortars (red star: mortar made with silica sand without air voids; blue star: mortar made with silica sand with air voids; green circle: mortar made with natural sand without air voids; cyan circle: mortar made with natural sand with air voids).

  - In the second regime, the p-wave velocity in the setting cement increases rapidly with time.
  - In the third regime, the p-wave velocity increases very slowly to reach an asymptotic value.

- A comparison of the experimental data with and without air voids shows that there was not much difference between the p-wave velocities in the first regime. However, as shown, the effect of the air voids on the p-wave velocity became more noticeable in the second and third regimes. In generally, the p-wave velocity in mortar was significantly reduced by the presence of air voids. The difference was about 600 to 800 m/s.
- There were also noticeable differences in the measure p-wave velocity for the mortar made with the silica sand compared to that made with the natural sand. The p-wave velocities of mortars made with natural sand were higher than those made with silica sand. This was because the natural sand had a larger aggregate size than the silica sand.

In the above set of measurements, a pair of Olympus Panametrics-NDT V101 ultrasonic contact transducers (with a resonance frequency of about 1 MHz) was used as both the source and receiver. An ultrasonic signal was sent from an Olympus Panametrics-NDT pulser-receiver (5077PR). The received signal was connected to a Tektronix digital oscilloscope (TDS2014B). Figure 2.2b shows a photograph of the experimental test rig.

### 4.2 Ultrasonic Characterization of Concrete in Its Early Hours of Hydration

In the next set of preliminary measurements, 4"-thick fresh concrete specimens were prepared using the following composition: (a) 0.75 kg of cement, (b) 0.12 kg of fly ash, (c) 366 ml of water, (d) 1.55 kg of fine aggregate, and (e) 2.05 kg of coarse aggregate. A single dose (0.2 ml) or double dose (0.4 ml) of AEAs was added to the water before it was mixed with the concrete. The constituents were mixed according to the established national standards (ASTM C192/C). A larger specimen holder (see Figure 2.3) was used; and a pair of ultrasonic transducers (Olympus Panametrics-NDT ultrasonic contact-type transducers: V101-RM) was used as the source and receiver. Each of these transducers, which were operated with a resonant frequency of 500 kHz, had a diameter of 1" (see Figure 2.6 for the relative sizes of the different transducers used in the preliminary experiments).

Figure 4.2 shows the p-wave velocity versus the hydration time of the concrete with three different air-void contents. Because it was difficult to quantitatively control the amount of air voids added to a concrete sample, controlling the dosage of AEAs added to the sample was a convenient alternative. Hence, three independent sets of measurements were conducted, where

(i) no AEA was added,
(ii) a single dose of the AEA was added, and
(iii) a double dose of the AEA was added.

to the concrete sample. A nominal control of the volume of air voids introduced to the samples was provided by specifying the amount of AEA added to the sample. However, the exact amounts of air voids introduced in the concrete samples for different dosages, which were expressed in terms of porosity, were not known in advance.

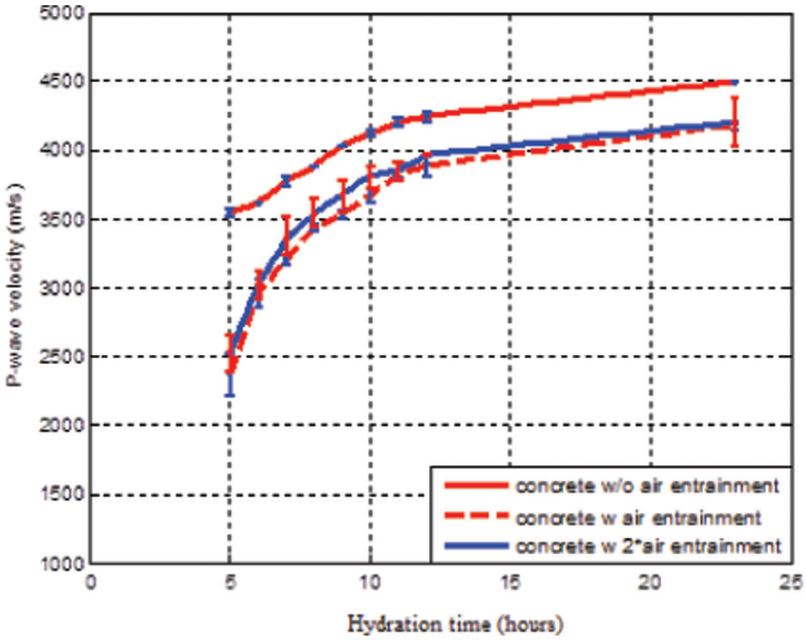


**Figure 4.2** Comparison of p-wave velocity versus setting time for different types of concrete with error bar (red solid line: concrete without air entrainment; red dashed line: concrete with one dose of air entrainment; blue solid line: concrete with two doses of air entrainment).

Two to four separate measurements were conducted for each of the conditions listed above, (i), (ii), and (iii). In these measurements, the p-wave velocities were recorded for different time periods after the initial mixing of the concrete samples. Figure 4.2 shows the mean p-wave velocity plotted against the time period after the initial mixing.

The coarse aggregates were present in the concrete but absent in the mortars. Hence, the p-wave velocity in the concrete was significantly higher than that measured in the mortars. For instance, the measured p-wave velocity in fresh concrete at the 5$^{th}$ hour was about 3500 m/s but it was only about 2200 m/s for mortars with natural sand and about 1500 m/s for mortars with silica. All of the measured results were based on samples without large-scale air voids. Comparable results were also observed for samples mixed with AEAs.

Similar to the performance of the mortars, the presence of air voids in concrete tended to reduce the p-wave velocity. There was a clear trend that the amount of air voids could be measured by monitoring the change in the p-wave velocity, although additional studies are needed to correlate the change in the p-wave velocity with the amount of air voids in the concrete. It was demonstrated from the measured results that the acoustic power for the 500-kHz ultrasound probe was insufficient to penetrate the fresh concrete within the first 5 h of the initial mixing. As a result, no reliable data were obtained for the measured p-wave velocities during this initial period.

In the period between the 5$^{th}$ hour and 12$^{th}$ hour, the rate of increase in the p-wave velocity was higher than that for the period after the first 12 h. The p-wave velocity tended to settle at a constant value when the concrete solidified. Again, the p-wave velocity for solid concrete will be dependent on the amount of air voids in the sample.

The p-wave velocities of the ultrasound transmitted through concrete samples with different air porosities could be distinguished by using the acoustical method. However, the amount of porosity in a sample cannot be established solely by acoustical means at the present stage. Therefore, the use of an air-void analysis system was proposed for measuring the air voids in solid concrete according to the established standards (*13*). This standard method specifies procedures for the microscopic determination of the air content of hardened concrete, as well as the specific surface, void frequency spacing factor, and paste-air ratio of the air-void system in the hardened concrete. These details will be presented in Section 4.4.

### 4.3 Ultrasonic Characterization of Fresh Cementitious Materials

Based on the preliminary experiments on cement and concrete, a revised experimental test rig was developed, as shown in Figure 2.4a. It was constructed from plexiglass and rubber to hold a 4"-thick cementitious (concrete or mortar) specimen. To reduce the effect of multiple reflections from the bottom edges of the experimental rig, the inner blocks contained four rubber spacers, each with a thickness of about 1". A pair of Ultran ultrasonic transducers, each with a diameter of 1.25", was used throughout the duration of the measurements unless otherwise indicated. The resonance frequencies of these two transducers are 140 kHz (GRD140) and 200 kHz (GRD200), respectively. The GRD140 was used as a transmitter, and the GRD200 was used as a receiver. This apparent mismatched configuration provided an improved sensitivity across a wide range of frequencies.

Mortar was recommended for the initial tests because of the dimensions of the constructed test rig. Several different compositions of cement, water, and silica sand were used in the preparation of the mortar specimens. Various concentrations of AEAs were added to the water prior to mixing to adjust the desired air content. The mixing procedures were implemented according to ASTM standards. Figure 4.3 shows a typical specimen that was removed from the test rig after setting.

The air content of a specimen was measured via two independent methods, in addition to the ultrasonic measurements. The first method is known as the isopropyl-alcohol method (based on Ref. (*49*)). Figure 4.4 shows an air indicator and the brass cylinder tube used in the tests. This method provides a rough estimate of the air content in fresh mortars, but it also relies on the skill of the technician. Because the measured results were rather inconsistent across the different tests conducted from one day to the next, this method was not used in practice.

An alternative method for measuring the air content of a fresh mixture was based on the measurement of the weight of a standard unit (a 400-ml fresh mortar specimen). Three different layers of the test specimen were poured into a standard test cylinder in succession. Each layer was tampered, and any excess mortar was removed from the topmost layer. The weight of the unit

**Figure 4.3** Hardened mortar specimen.

**Figure 4.4** Air indicator and brass cylinder tube used for measurement of air content.

was measured, and the air content was calculated based on the known composition of the test specimen. It was found that the determination of air content using this method gave more consistent results. Hence, it was chosen to give an initial assessment of the air content in a specimen for this set of experiments.

A similar tampering process was used to layer the fresh mortar into the test rig for ultrasonic characterization. The time-domain signal was acquired using a digital oscilloscope (Tektronix TDS2014B) controlled via MATLAB's VISA-USB interface. This enabled automated data acquisition and data processing to take place almost instantaneously. An onset time selection algorithm based on the energy density of the signal was applied to find the vicinity of the first onset. Then, a zero-crossing search was used to identify the true onset time.

Using the numerical algorithm described in Section 3.1, the onset times for different specimens were determined. Based on these onset times, the p-wave velocities of the ultrasound transmitted through the specimen at a series of hydration times were calculated. Figure 4.5 shows a signal smoothed using a five-point triangular moving average to preserve the position of the amplitude data. It can be seen that even at an elapsed time of 35 min, it is still very difficult to gauge the onset time because of the noisy ripples and relatively high attenuation rates. To make matters worse, as the air content increased, the signal became more attenuated. Using an amplitude-based approach made it possible to detect a fairly consistent onset time when the air content was low (below ~11%). At higher air content, the detection rate could be off by about half a cycle of the sinusoidal oscillation shown in Figure 4.5.

Figure 4.6 shows the plots of the p-wave velocities for the cement specimens for the initial 2 h of hydration time. It was much easier to determine the onset times at higher setting times because the hardening of the test specimen increased the signal strength. A clustering of results is observed within the error bounds for each of the test specimens. In these plots, the air content percentage is determined by the weight of a standard unit (a 400-ml fresh mortar specimen). More accurate methods for determining the air content (such as optical characterization) will be required to confirm the percentage of air content in this set of experiments. Details of the optical characterization method will be described in the following section.

### 4.4 Optical Characterization of Cementitious Specimens

As previously mentioned, optical characterization has become the preferred technique for determining the air content of a test specimen because it provides a more consistent, reproducible result than any of the other methods previously discussed. The drawback is the need to wait until the specimen has thoroughly hardened before slicing it for examination. Typically, sliced specimens are polished and scanned based on the relevant ASTM standards. The optical characterization method provides an independent confirmation of the air content in a cementitious specimen found by the ultrasound technique. To validate this optical method, a model comparison was performed among the method, the algorithm based on MATLAB's IPT, and the BC script according to Refs. (*46,51*).

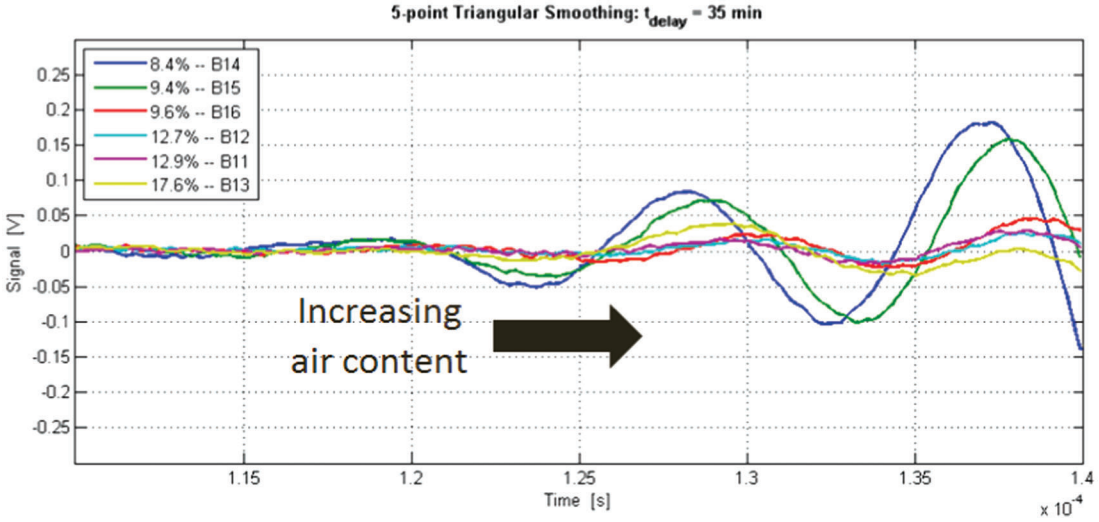


**Figure 4.5** Representative time-domain signals after 35 min has elapsed after mixing.

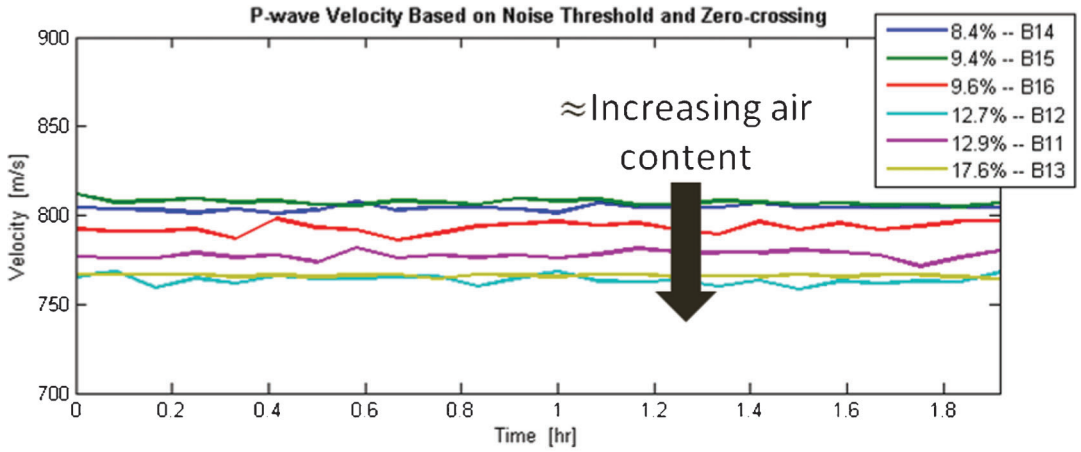


**Figure 4.6** Plot of p-wave velocity of specimen versus hydration time for different air content. The air content was determined by the weight of the mortar specimen.

Table 4.1 shows an excerpt of the data obtained. Based on the results, the IPT algorithm consistently underpredicted the air content of the test specimens compared to the BC script. Closer inspection reveals that the relative spread in the detected values between slices of the same samples was tighter when the IPT algorithm was used.

For slices of the same test specimen, the air content was not expected to vary by more than a few percent. Because the BC script relies on a statistical approach, the spread in the results can be quite high when non-representative sampling regions are taken. On the other hand, the IPT algorithm attempts to maximize the sampling area via a non-rectangular windowing approach. It also analyzes each individual pixel in the scanned image to provide a more physically meaningful output that uses all of the available information. Defects within the sampling region can be confirmed visually and removed prior to a subsequent run of the algorithm. This iterative process allows more accurate results to be obtained and verified.

Comparing the optical analysis results to the unit weighting method, neither the BC script nor the IPT algorithm were able to achieve the high concentration of air content calculated by the unit weighting method. The maximum level predicted by the IPT algorithm was

TABLE 4.1
**Comparison of BC script outputs with IPT algorithm for mortar specimens***

| Specimen Name | Unit Weighting Method (%) | BC Air Content (%) | IPT Air Content (%) | BC Average (%) | IPT Average (%) | Percent Difference (%) |
|---|---|---|---|---|---|---|
| 6-29-S11-I | 6.7 | 6.63 | 6.55 | 8.00 | 6.65 | 20.3 |
| 6-29-S11-II | | 9.36 | 6.76 | | | |
| 6-29-S12-III | 9.8 | 10.13 | 8.03 | 9.77 | 8.72 | 12.04 |
| 6-29-S12-IV | | 9.4 | 9.41 | | | |
| 6-29-S13-V | 11.9 | 13.04 | 11.4 | 11.59 | 10.55 | 9.86 |
| 6-29-S13-VI | | 10.13 | 9.72 | | | |
| 6-30-S14-I | 14 | 11.68 | 9.66 | 10.75 | 9.44 | 13.88 |
| 6-30-S14-II | | 9.81 | 9.22 | | | |
| 7-01-S15-I | 14.3 | 10.52 | 9.57 | 11.04 | 9.78 | 12.88 |
| 7-01-S15-II | | 11.55 | 10.0 | | | |
| 7-05-S16-III | 15.7 | 14.97 | 11.63 | 14.71 | 11.36 | 29.49 |
| 7-05-S16-IV | | 14.45 | 11.10 | | | |
| 7-05-S17-V | 17.6 | 12.08 | 10.18 | 11.48 | 10.36 | 10.82 |
| 7-05-S17-VI | | 10.87 | 10.54 | | | |
| 7-05-S18-I | 20.4 | 11.61 | 9.09 | 11.23 | 9.30 | 20.75 |
| 7-11-S18-II | | 10.84 | 9.50 | | | |

*The analysis was performed on individual slices of the same test specimen. Then, an average was found for slices of the same specimen. A threshold level of 140 was set within the IPT algorithm. Percentage differences are referenced to the IPT air content values obtained.

11.36%, which was considerably lower than the other two prediction methods. Some of the errors might be attributed to the correspondence between a volumetric approach and one based on surface area. It is more valid to compare the two surface area sampling approaches. Overall, the IPT algorithm provided results that were about 16% lower than those obtained via the BC script.

### *4.4.1 Air-Void Distribution Analysis*

One of the capabilities of the IPT algorithm is its ability to sort the air voids by size. Because no watershed algorithm has been implemented to segment larger bubbles into several smaller bubbles based on shape, the following results can still be improved upon, but this was not done in the present study. Figure 4.7 shows the results obtained for various mortar specimens. The air content percentages were obtained from the IPT algorithm.

As seen in the figure, much of the behavior in the middle section of the diagram remains relatively constant as the air content is varied. Much larger changes are observed in the number of smaller-sized air voids. The results for the larger-sized air voids are deceptive on a logarithmic scale because of their low number of occurrences (about 1,000 times less than the smallest air-void bin). Hence, much of the contribution to the total air content is dependent on the small and mid-sized air voids.

Coincidentally, at an air-void area of approximately $1.2 \times 10^{-2}$, the contours of the number density agree quite well with the predicted air content of the various specimens. The low air content curves tend to be clustered toward the lower number of occurrences. As the air content is increased, the contours shift upward. On the other hand, no clear trends are observed for the rest of the data.

Based on the results from Nambiar and Ramamurthy (*47*), the cumulative frequency distribution at low dosages of air entrainment tends to be more uniform than at the higher dosages in cement-fly ash mixtures. This trend is seen to be less dominant in cement-sand mixes, which are the subject of the current feasibility study. It is suggested that using a finer filler material such as fly ash allows the bubbles in the paste to be coated more evenly, which helps reduce the potential for bubbles to merge and/or overlap. It should be noted that the computation of the spacing factor has not yet been implemented in the IPT algorithm. Hence, no further comparisons can be made.

Using the information obtained from the connected element analysis regarding the perimeter of each air void, the shape factor can also be computed. The shape factor (*SH*) is defined as:

$$SH = \frac{P^2}{4\pi A} \tag{3}$$

Where $P$ is the perimeter of the air void and $A$ is the area of the object. The shape factor is unity for a circular air void and is larger for irregularly shaped voids.

### *4.4.2 Coarse Aggregate Image Processing*

Several different image processing techniques have been explored to characterize coarse aggregate specimens. The feasibility of developing a classification routine has been verified. However, the sensitivity of the detection algorithm still needs to be improved for more reliable outputs.

For basic sample analysis, the numerical algorithms for the IPT techniques and the mortar analysis routines perform quite well because they are essentially the same methods. When processing coarse aggregates, an

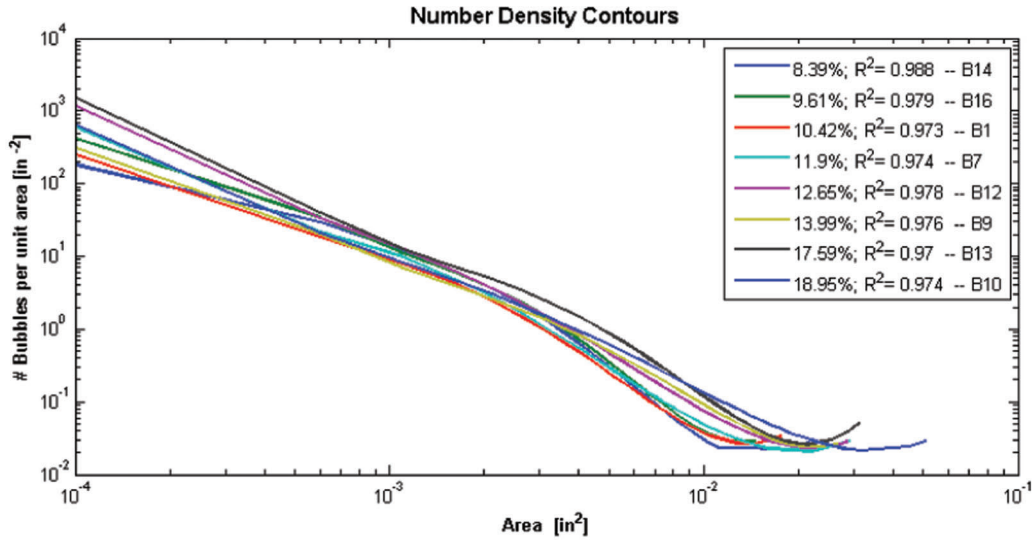


**Figure 4.7** Bubble size distribution diagram for mortar specimen. The last blue curve corresponding to 18.95% extends to higher areas. Each individual curve represented on the diagram has been curve-fitted to its bubble size distribution via a fifth-order polynomial.

operator is needed to fill in the aggregate grains visually. More sophisticated methods are under development to aid the user in performing the task more effectively.

From the binary image, a *bwdist* subroutine in MATLAB can be applied to compute the spacing factor. This subroutine computes the distance between each background pixel to the nearest non-zero object (i.e., air void in the binary image representation). A better understanding of the two-dimensional spacing computation in the presence of aggregate is needed to proceed with the design of the numerical algorithm.

With a classification routine, additional parameters can be extracted from the scanned image. The statistics for a large aggregate can be obtained. One interesting application would be to identify the number of air voids that nucleate near the grain boundaries of the coarse aggregate. Another might be to determine the size distribution and mean free path between pieces of aggregate throughout the test specimen. Presumably, the ultrasonic signature of the air voids and solid suspension particles in the test specimen plays an important role in scattering the incident acoustic wave within the first few hours of hydration.

## 4.5 Limitation on Use of Ultrasound in Fresh Concrete

In Section 4.3, fresh mortars were used in the experimental test rig to determine the p-wave velocities transmitted through specimens within the first two hours of hydration time. The next step involved the use of fresh concrete specimens in the experiments. It was found that the detection threshold for acoustical signals propagated through the fresh concrete was very low. In some instances, especially when working with coarse aggregate specimens, insufficient contact between the ultrasound probe and test specimen was experienced. Variability in the time-domain signals for the same sample composition and preparation procedures was experienced when some of the previous experiments were repeated to test the new data acquisition system. This led to an investigation of the possible errors from the experimental test rig and an improved design for the existing experimental test fixture. These are described as follows.

### *4.5.1 Experimental Error*

In the ultrasonic measurements, ensuring good contact between the ultrasonic transducers and test specimen was essential. Typically, ultrasonic gel was applied at the surface of the transducers to ensure full contact with the test specimens. Care was taken to remove any air voids in the ultrasonic gel within the active area of the transducers. A piece of thin film was used in each of the transducers in the experimental test rig. These thin films were used to protect the transducers from direct contact with the fresh concrete, which could damage them.

Signal quality was crucial because the ultrasonic pulse contained multiple lobes when it arrived at the receiver. The triggering algorithm could only separate the data from the noise when the actual data were distinguishable from the noise. In the signal shown in Figure 4.8, a signal can be distinguished from the background noise, but the distinguishing point (i.e., onset time) is ambiguous because it depends on the selection of the triggering algorithm and its implementation. Suppose the signal is further attenuated because of a misalignment of the transducers, additional sample thickness, coarse aggregate, or poor contact between the relevant interfaces in the propagation pathway. The signal amplitudes would decrease and low-amplitude sections of the signal would disappear into the noise. When this occurs, the next prominent peak in the signal pulse would be detected by the triggering algorithm instead of the actual leading edge of the signal. In a p-wave velocity analysis, this would correspond to a longer onset time or a slower p-wave velocity than the actual value.

When analyzing small signals under low signal-to-noise conditions, this false-positive effect can become substantial. Low signal levels always occur during the first few hours of hydration because of the presence of a fluid phase in the specimen. A low signal level can also occur in a specimen with high air content because of an increase in the scattering effects by the air voids. Thus, large errors are expected in the first few hours of setting, but the error should be biased toward underpredictions of the actual p-wave velocity.

### *4.5.2 Improved Experimental Test Rig for Fresh Concrete*

Because of difficulties in obtaining a consistent time-domain signal across various experiments, even when performed on the same day, it was determined that the specimen container needed to be revised. More consistent methods for specimen preparation were also explored. Initially, the experimental test fixture

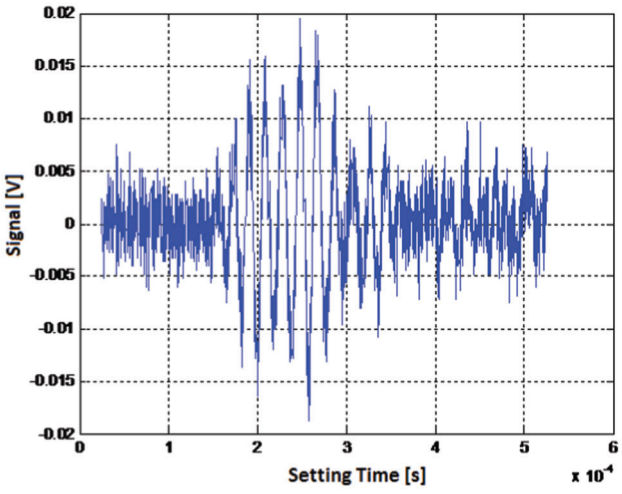


**Figure 4.8** Time history of typical cementitious specimen.

revisions were prompted by alignment issues with the ultrasound transducers (sound source and receiver) and inconsistent sample thicknesses.

A revised test fixture was assembled and modified until it was ready for bench testing. The initial results from the new test fixture demonstrated that no ultrasonic signal was detected through a 4"-thick gap during the first two hours of testing. By applying a large amount of pressure to the sensor plates, a small signal was detectable. It was eventually discovered that the old rubber sidewall test fixture was not ideal for testing low p-wave velocities because of structural propagation effects.

The rubber sidewall test fixtures, which were used in the majority of the earlier tests, were based on a configuration found in other studies. It was subsequently found that a layered plexiglass sidewall construction provided sufficient vibration isolation to attenuate the structurally propagated signal path. Figure 2.3 shows the old test fixture that was used in our earlier ultrasound experiments for cement paste. In retrospect, this design performed much better than the rubber sidewall construction that replaced it.

The main concern with using a rigid material for the sidewall construction of the improved test fixture was the possibility of short-circuiting the acoustic path via a structural transmission path. This issue was inadvertently resolved by placing the ultrasonic transducers in a metal collar and then embedding the mounted sensor in a thick plexiglass plate (for alignment) in the new design of the experimental test fixture. Multiple panels of plexiglass were sandwiched between the two sensor plates in the assembled test rig. The net result was the uncoupling of the acoustic and structural propagation paths. A photograph of the improved test rig is shown in Figure 2.7.

Circular apertures were cut in the thin sidewall sections to allow direct access to the concrete test specimens. A layer of film was placed between the specimens and sensor to seal the aperture and prevent leakage. Additionally, ultrasonic gel was applied between the thin film and transducers to ensure adequate sensor contact. The sensor plates were aligned using three metal pins attached to each specimen container. Then, four clamps were applied to the corners of the test fixture to ensure a tight fit for the measurements. After the data acquisition step, the sensor plates could be removed and reused in subsequent tests.

### *4.5.3 Feasibility of Optical Characterization of Fresh Concrete*

With the revised test rig and improved instrumentation, more experiments were conducted to examine the feasibility of ultrasonic characterization techniques. It was found that the maximum thickness for signal propagation within the first 20 min of hydration was of the order of 0.4". A more powerful square wave pulser (Ritec SP-801A), along with a step-up transformer, was sourced from Ritec to gauge the maximum sample thickness and evaluate the feasibility of testing coarse aggregate samples. The step-up transformer allowed up to a three-fold increase in the amplifier output; the transformer was custom designed to function well beyond 100 kHz. Instead of using a pair of mismatched transducers (140 kHz and 200 kHz), a pair of identical transducers (Ultran GRD140) was used, with a resonance frequency of 140 KHz. The SP-801A allowed the pulsing frequency to be fine-tuned to match half of the resonance frequency of the GRD140.

TABLE 4.2
**Evaluation of SP-801A paired with 1:2 and 1:3 step-up transformers***

| | | | |
|---|---|---|---|
| Pulser Output Voltage [V] | −400 | −800 | −1,200 |
| SP-801A Measured [V] | 0.30 | 0.60 | 0.90 |
| 5077PR Measured [V] | 0.225 | 0.38 | 0.49 |
| Percent Improvement [%] | 33 | 58 | 84 |

*The SP-801A is tuned to 70 kHz, and the 5077PR is tuned to 100 kHz.

The net result was a maximum driving voltage of −1200 V being supplied to the transmitter. Additionally, the step-up transformer could be placed between the transmitter and the output of the 5077PR to increase its output. Performing a bench test with a 4" air-gap and measuring the amplitude of the second positive lobe yielded the results shown in Table 4.2. The receiver gain was set to +20 dB for the duration of the air-gap bench tests.

Based on the results at the lowest pulser voltage setting, there was a 33% improvement in the signal amplitude as a result of the resonance matching effect. Larger improvements were obtained at the maximum setting of −1,200 V. The system described above was the best system that could be acquired at the time of the feasibility study. There was a maximum voltage that the transducers were capable of handling before the piezoelectric crystals degraded or the internal fail-safe circuitry was triggered. Typically, lower frequency transducers have thicker crystal elements, which make them more resistant to high voltages. With the best system, it is estimated that ultrasound sound signals can penetrate a maximum thickness of a 0.6" of fresh concrete. Given the typical concrete specimen thickness of 4", it seems unlikely that an ultrasound through-transmission method can be used to determine the air voids in fresh concrete within the limit of 30 min of hydration time.

## 5. CONCLUSIONS

The ultimate goal of this feasibility study was to identify whether coarse aggregate specimens can be characterized within the first hour of hydration. Based on the results obtained from the available instrumentation, the largest sample thickness for signal transmission is of the order of 0.6". For mortar specimens, this sample thickness may be acceptable. However, this

thickness is not acceptable for a fresh concrete specimen. This is because the minimum sample thickness needs to be several times larger than the characteristic length scale of the aggregate to obtain a representative sampling.

The latest experimental setup demonstrated the feasibility of using a step-up transformer and a set of tuned transducers to significantly increase the time-domain signal amplitude at minimal additional costs. To overcome the signal quality issues encountered, larger active area transducers with higher amplitude outputs might be sourced. Although the desired sample thickness of 4" was not achieved during the first two hours of hydration, this sample thickness constraint may be relaxed by switching to a larger active area transducer. The effective result would be sampling a comparable volume of the test specimen, but at a lower sample thickness.

Another goal of the present project was the development of image processing techniques during the refinement process in the design of the experimental test fixture. No conclusive time-domain results were obtained within the first few hours of hydration. On the other hand, more reliable data were recorded beyond this time window.

Based on the results obtained from the IPT algorithm, expanded capabilities can be addressed by processing the entire high-resolution image. These capabilities may reduce the time and effort needed to prepare each specimen for air-void analysis. In turn, more specimens can be analyzed to generate statistically representative predictions. Preliminary results show promise that a coarse aggregate identification filter based on high sensitivity edge detection combined with color image enhancement techniques would yield a semi-automatic classification system. The image processing algorithms can also be applied to other optical characterization projects for the estimation of other pertinent parameters of cementitious materials.

## REFERENCES


1. Mielenz, R. C., V. E. Wolkodoff, J. S. Backstrom, and H. L. Flack. Origin, Evolution, and Effects of the Air Void System in Concrete. *Journal of the American Concrete Institute*, Vol. 30, 1958, pp. 95–121.
2. Powers, T. C. Void Spacing as a Basis for Producing Air Entrained Concrete. *Journal of the American Concrete Institute*, Vol. 25, 2005, pp. 1463–1471.
3. Du, L., and K. J. Folliard. Mechanisms of Air Entrainment in Concrete. *Cement and Concrete Research*, Vol. 35, 2005, pp. 1463–1471.
4. Powers, T. C. The Air Requirement of Frost-Resistant Concrete. *Proceedings of the Highway Research board*, Vol. 29, 1949, pp. 184–211.
5. Synder, K. A. A Numerical Test of Air Void Spacing Equations. *Advanced Cement Based Materials*, Vol. 8, 1998, pp. 28–44.
6. Philleo, R. E. A Method for Analyzing Void Distribution in Air Entrained Concrete. *Cement Concrete Aggregates*, Vol. 5, 1983, pp. 128–130.
7. Attiogbe, E. K. Mean Spacing of Air Voids in Hardened Concrete. *ACI Materials Journal*, Vol. 90, 1993, pp. 174–18.
8. Pleau, R., and M. Pigeon. The Use of the Flow Length Concept to Assess the Efficiency of Air Entrainment with Regards to Frost Durability. 1. Description of the Test Method. *Cement Concrete Aggregates*, Vol. 18, 1996, pp. 19–29.
9. Pleau, R., M. Pigeon, L. Laurencot, and R. Gagne. The Use of the Flow Length Concept to Assess the Efficiency of Air Entrainment with Regards to Frost Durability. 2. Experimental results. *Cement Concrete Aggregates*, Vol. 18, 1996, pp. 30–41.
10. Attiogbe, E. K. Predicting Freeze-Thaw Durability of Concrete: A New Approach. *ACI Mater. J.*, Vol. 93, 1996, pp. 457–464.
11. Delatte, N. *Concrete Pavement Design, Construction, and Performance*. Taylor & Francis, London and New York, 2008.
12. Hulshizer, A. J. Air-Entrainment Control or Consequences. *Concrete Institute*, Vol. 18, 1997, pp. 38–40.
13. American Society for Testing and Materials. ASTM C 457. Standard Test Method for Microscopical Determination of Parameters of the Air-Void System in Hardened Concrete. In *Annual Book of the American Society of Testing Materials Standards*, ASTM, 1991, pp. 229–241.
14. Laurencot, J. L., R. Pleau, and M. Pigeon. The Microscopical Determination of Air-Void Characteristics in Hardened Concrete: Development of an Automatic System Using Image Analysis Techniques Applied to Micro-computers. *Proceedings of the 14th International Conference of Cement Microscopy*, Costa Mesa, USA, 1992, pp. 259–273.
15. Zalocha, D., and J. Kasperkiewica. Estimation of the Structure of Air Entrained Concrete Using a Flatbed Scanner. *Cement and Concrete Research*, Vol. 35, 2005, pp. 2041–2046.
16. Pigeon, M., and R. Pleau. *Durability of Concrete in Cold Climates*. Chapman & Hall, London, 1995.
17. Price, B. Measuring Air Voids in Fresh Concrete. *Concrete*, Vol. 30, 1995, pp. 29–31.
18. Soshiroda, T., K. Voraputhaporn, and Y. Noaki. Early-Stage Inspection of Concrete Quality in Structures by Combined Nondestructive Method. *Materials and Structures*, Vol. 39, 2006, pp. 149–160.
19. Philippidis, T. P., and D. G. Aggelis. Experimental Study of Wave Dispersion and Attenuation in Concrete. *Ultrasonics*, Vol. 43, 2005, pp. 584–595.
20. Punurai, W., J. Jarzynki, J. Qu, J. Y. Kim, L. J. Jacobs, and K. Kurtis. Characterization of Multi-scale Porosity in Cement Paste by Advanced Ultrasonic Techniques. *Cement and Concrete Research*, Vol. 37, 2007, pp. 38–46.
21. Kim, J. H., S. P. Shah, Z. Sun, and H. G. Kwak. Ultrasonic Wave Reflection and Resonant Frequency Measurements for Monitoring Early-Age Concrete. *ASCE*, Vol. 9, 2009, pp. 476–483.
22. Robeyst, N., E. Gruyaert, C. U. Grosse, and N. D. Bellie. Monitoring the Setting of Concrete Containing Blast-Furnace Slag by Measuring the Ultrasonic P-Wave Velocity. *Cement and Concrete Research*, Vol. 38, 2008, pp. 1169–1176.
23. Kmack, R. M., K. E. Kurtis, L. J. Jacobs, and J. Y. Kim. Assessment of Air Entrainment in Fresh Cement Paste Using Ultrasonic Nondestructive Testing. *Journal of ASTM International*, Vol. 7, 2010.
24. Zhu, J., S. H. Kee, D. Han, and Y. T. Tsai. Effects of Air Voids on Ultrasonic Wave Propagation in Early Age

Cement Pastes. *Cement and Concrete Research*, Vol. 41, 2011, pp. 872–881.
25. Chekroun, M., L. Le Marrec, O. Abraham, O. Durand, and G. Villain. Analysis of Coherent Surface Wave Dispersion and Attenuation for Non-Destructive Testing of Concrete. *Ultrasonics*, Vol. 49, 2009, pp. 743–751.
26. Punurai, W., J. Jarzynki, J. Qu, K.E. Kurtis, and L.J. Jacobs. Characterisation of Entrained Air Voids in Cement Paste with Scattered Ultrasound. *NDT&E International*, Vol. 39, 2006, pp. 514–524.
27. Aggelis, D. G., D. Polyzos, and T. P. Philippidis. Wave Dispersion and Attenuation in Fresh Mortar: Theoretical Predictions versus Experimental Results. *Journal of the Mechanics and Physics of Solids*, Vol. 53, 2005, pp. 857–883.
28. Chaix, J. F., V. Garnier, and G. Corneloup. Ultrasonic Wave Propagation in Heterogeneous Solid Media: Theoretical Analysis and Experimental Validation. *Ultrasonics*, Vol. 44, 2006, pp. 200–210.
29. Reinhardt, H. W., C. U. Grosse, and A. T. Herb. Ultrasonic Monitoring of Setting and Hardening of Cement Mortar–A New Device. *Materials and Structures*, Vol. 33, 2000, pp. 580–583.
30. Reinhardt, H. W., and C. U. Grosse. Continuous Monitoring of Setting and Hardening of Mortar and Concrete. *Construction and Building Materials*, Vol. 18, 2004, pp. 145–154.
31. Ozturk, T., O. Kroggel, P. Grubl, and J. J. Popovics. Improved Ultrasonic Wave Reflection Technique to Monitor the Setting of Cement-Based Materials. *NDT&E International*, Vol. 39, 2006, pp. 258–263.
32. Kolluru, S. V., J. S. Popovics, and S.P. Shah. Determining Elastic Properties of Concrete Using Vibrational Resonance Frequencies of Standard Test Cylinders, Cement, Concrete, and Aggregates. *Cement Concrete Aggregates*, Vol. 22, 2000, pp. 81–89.
33. Sayers, C. M., and R. L. Grenfell. Ultrasonic Propagation through Hydrating Cements. *Ultrasonics*, Vol. 31, 1993, pp. 147–153.
34. Sayers, C. M., and A. Dahlin. Propagation of Ultrasound through Hydrating Cement Pastes at Early Times. *Advanced Cement Based Materials*, Vol. 1, 1993, pp. 12–21.
35. Aggelis, D. G., and T. P. Philippidis. Ultrasonic Wave Dispersion and Attenuation in Fresh Mortar. *NDT&E International*, Vol. 37, 2004, pp. 617–631.
36. In, C. W., J. Y. Kim, L. J. Jacobs, and K. E. Kurtis. Characterization of Dispersive Ultrasonic Rayleigh Surface Waves in Asphalt Concrete. *Review of Quantitative Nondestructive Evaluation*, Vol. 27, 2008, pp. 1333–1338.
37. Piwakowski, B. A., Fnine, M. Goueygou, and B. Buyle-Bodin. Generation of Rayleigh Waves into Mortar and Concrete Samples. *Ultrasonics*, Vol. 42, 2004, pp. 395–402.
38. Algernon, D., B. Grafe, F. Mielenz, B. Kohler, and F. Schubert. Imaging of the Elastic Wave Propagation in Concrete Using Scanning Techniques: Application for Impact-Echo and Ultrasonic Echo Methods. *Journal of Nondestructive Evaluation*, Vol. 27, 2008, pp. 83–97.
39. Chekroun, M. L., Le Marrec, B. Lombard, J. Piraux, and O. Abraham. Comparison between Multiple Scattering Methods and Direct Numerical Simulations for Elastic Wave Propagation in Concrete. *Proceedings in Physics*, Vol. 28, 2009, pp. 317–327.
40. American Society for Testing and Materials. C231-04. Standard Test Method for Air Content of Freshly Mixed Concrete by the Pressure Method. In *Annual Book of ASTM Standards: Volume 04.02, Concrete and Aggregates*. ASTM, West Conshohocken, PA.
41. American Society for Testing and Materials. C173-01. Standard Test Method for Air Content of Freshly Mixed Concrete by the Volumetric Method. In *Annual Book of ASTM Standards*. ASTM, West Conshohocken, PA.
42. American Society for Testing and Materials. C138-01a. Standard Test Method for Density (Unit Weight), Yield, and Air Content (Gravimetric) of Concrete. In *Annual Book of ASTM Standards*. ASTM, West Conshohocken, PA.
43. Walker, H. N., D. S. Lane, and P. E. Stutzman. *Petrographic Methods of Examining Hardened Concrete: A Petrographic Manual, Revised 2004*. Publication FHWA-HRT-04-105. Federal Highway Authority, 2006.
44. Jana, D. A Round Robin Test on Measurements of Air Void Parameters in Hardened Concrete by Various Automated Image Analyses and ASTM C 457 Methods. Presented at the 29th Conference on Cement Microscopy, Quebec City, Canada, May 20-24, 2007.
45. Pade, C., U. H. Jakobson, and J. Elsen. A New Automatic Analysis System for Analyzing the Air Void System in Hardened Concrete. In *Proceedings of the 24th International Conference on Cement Microscopy*, International Cement Microscopy Association, San Diego, CA, 2002, pp. 204–213.
46. Peterson, K., L. Sutter, and M. Radlinski. The Practical Application of a Flatbed Scanner for Air Void Characterization of Hardened Concrete. *Journal of ASTM International*, Vol. Vol. 6, 2009.
47. Nambiar, E. K., and K. Ramamurthy. Air-Void Characterisation of Foam Concrete. *Cement and Concrete Research*, Vol. 37, 2007, pp. 221–230.
48. Lee. H. K, K. M. Lee, Y. H. Kim, H. Yim, and D. B. Bae. Ultrasonic In-Situ Monitoring of Setting Process of High-Performance Concrete. *Cement and Concrete Research*, Vol. 34, 2004, pp. 631–640.
49. AASHTO T137-04. *Standard Method of Test for Air Content of Hydraulic Cement Mortar*. American Association of State and Highway Transportation Officials, Washington, D.C. Also see ASTM C185-02. Standard Test Method for Air Content of Hydraulic Cement Mortar. ASTM (American Society of Testing and Materials) International, West Conshohocken, PA.
50. Kurz, J. H., C. U. Grosse, and H. W. Reinhardt. Strategies for Reliable Automatic Onset Time Picking of Acoustic Emissions and of Ultrasound Signals in Concrete. *Ultrasonics*, Vol. 43, 2005, pp. 538–546.
51. Peterson, K., L. Sutter, and T. Van Dam. Air Void Analysis of Hardened Concrete with a High-Resolution Flatbed Scanner. *Proceedings of the 24th International Conference on Cement Microscopy*, San Diego, California, 2002, pp. 304–316.

## About the Joint Transportation Research Program (JTRP)

On March 11, 1937, the Indiana Legislature passed an act which authorized the Indiana State Highway Commission to cooperate with and assist Purdue University in developing the best methods of improving and maintaining the highways of the state and the respective counties thereof. That collaborative effort was called the Joint Highway Research Project (JHRP). In 1997 the collaborative venture was renamed as the Joint Transportation Research Program (JTRP) to reflect the state and national efforts to integrate the management and operation of various transportation modes.

The first studies of JHRP were concerned with Test Road No. 1—evaluation of the weathering characteristics of stabilized materials. After World War II, the JHRP program grew substantially and was regularly producing technical reports. Over 1,500 technical reports are now available, published as part of the JHRP and subsequently JTRP collaborative venture between Purdue University and what is now the Indiana Department of Transportation.

Free online access to all reports is provided through a unique collaboration between JTRP and Purdue Libraries. These are available at: http://docs.lib.purdue.edu/jtrp

Further information about JTRP and its current research program is available at: http://www.purdue.edu/jtrp

## About This Report

An open access version of this publication is available online. This can be most easily located using the Digital Object Identifier (doi) listed below. Pre-2011 publications that include color illustrations are available online in color but are printed only in grayscale.

The recommended citation for this publication is:

Li, K. M., B. N. Tong, and S. Liu. *Feasibility Study of In-situ Characterization of Size Distribution of Air Voids in Concrete Pavements*. Publication FHWA/IN/JTRP-2013/10. Joint Transportation Research Program, Indiana Department of Transportation and Purdue University, West Lafayette, Indiana, 2013. doi: 10.5703/1288284315212.